Masters Thesis

Mechanics R&D on Mighty Tracker prototype modules

Author:
Emad S Hamdani

Supervisor:
Prof. Marco Gersabeck

A dissertation submitted to the University of Manchester

for the degree of Master of Science by Research

In the

Department of Physics and Astronomy

Faculty of Science and Engineering

2023

{*Blank page*}

Contents

List of Figures

List of Tables

{*Blank page*}

Abstract

Mechanics R&D on Mighty Tracker prototype modules

by Emad S Hamdani

University Of Manchester
Department of Physics and Astronomy
Faculty of Science and Engineering

In preparation for the High-Luminosity LHC (HL-LHC) era, the LHCb experiment is undergoing a significant upgrade. A crucial element of this upgrade is the replacement of the radiation-damaged Scintillating Fibre (SciFi) Tracker with the Mighty Tracker. The Mighty Tracker is a hybrid detector that utilises both pixel and fibre technologies to achieve superior tracking capabilities at the increased luminosities expected at HL-LHC. This study focuses on the characterisation of prototype modules for the silicon pixel part of the Mighty Tracker, employing metrology, thermal analysis, and non-destructive evaluation techniques to inform the mechanical design.

Prototype modules for the silicon pixel detector within the LHCb experiment's upgraded Mighty Tracker were characterised using a combination of metrology, thermal simulations, and X-ray tomography. Non-contact 3D measurements ensured dimensional consistency (thickness, planarity) of co-cured carbon foam and fibre samples for robust module construction. Post-assembly metrology evaluated structural integrity. Thermal simulations, considering material properties, geometry, and cooling, optimised the number of cooling pipes required to maintain optimal operational temperatures. High-resolution X-ray tomography enabled visualisation of internal structures, allowing quantification of glue distribution, pipe diameters, and potential defects.

Metrology, thermal simulations, and X-ray tomography provided stringent quality control for the mechanical design of the silicon pixel detector modules. These techniques validated key assumptions about material properties, dimensional tolerances, and thermal management. The insights gained will guide refinements to the design and as-

sembly processes, ultimately ensuring the upgraded LHCb Silicon Tracker achieves its performance goals.

{*Blank page*}

Declaration of Authorship

Candidate Name: Emad S Hamdani

Faculty: Faculty of science and Engineering

Department: Department of Physics and Astronomy

Thesis Title: Mechanics R&D of Mighty Tracker prototype modules

This work represents the combined efforts of the author and his colleagues in the university of Manchester. Some of the content has been published elsewhere and/or presented to several audiences. No portion of the work referred to in the thesis has been submitted in support of an application for another degree or qualification of this or any other university or other institute of learning.

Signed:

Date:

Copyright Statement

(i) The author of this thesis (including any appendices and/or schedules to this thesis) owns certain copyright or related rights in it (the “Copyright”) and they have given the University of Manchester certain rights to use such Copyright, including for administrative purposes.

(ii) Copies of this dissertation, either in full or in extracts and whether in hard or electronic copy, may be made **only** in accordance with the Copyright, Designs and Patents Act 1988 (as amended) and regulations issued under it or, where appropriate, in accordance with licensing agreements which the University has from time to time. This page must form part of any such copies made.

(iii) The ownership of certain Copyright, patents, designs, trademarks and other intellectual property (the “Intellectual Property”) and any reproductions of copyright works in the dissertation, for example graphs and tables (“Reproductions”), which may be described in this dissertation, may not be owned by the author and may be owned by third parties. Such Intellectual Property and Reproductions cannot and must not be made available for use without the prior written permission of the owner(s) of the relevant Intellectual Property and/or Reproductions.

(iv) Further information on the conditions under which disclosure, publication and commercialisation of this dissertation, the Copyright and any Intellectual Property and/or Reproductions described in it may take place is available in the University IP Policy (see https://documents.manchester.ac.uk/DocuInfo.aspx?DocID=24420), in any relevant Dissertation restriction declarations deposited in the University Library, the University Library’s regulations (see https://www.library.manchester.ac.uk/about/regulations/) and in the University’s policy on Presentation of Dissertation.

Acknowledgments

I would like to express my deepest gratitude to the individuals who have contributed to the successful completion of my Master's thesis. Their guidance, support, and expertise have been invaluable throughout this journey.

First and foremost, I extend my heartfelt appreciation to my supervisor, Marco. Your unwavering support, insightful guidance, and dedication to the pursuit of knowledge have been truly inspiring. Your mentorship has played a pivotal role in shaping the direction of my research and has enriched my academic experience. I am also grateful to my co-supervisors, Oscar, Stefano, and Alex, for their invaluable contributions to this thesis. Your expertise, feedback, and willingness to share your knowledge have greatly enhanced the quality of my work. Your collective insights have broadened my perspective and deepened my understanding of the subject matter.

I would like to acknowledge the entire academic community at the University of Manchester, whose resources, facilities, and collaborative spirit have provided an enriching environment for research and learning. I extend my appreciation to my family and friends for their unwavering encouragement and understanding during the demanding phases of this academic endeavour.

Lastly, I would like to thank all the participants and individuals who generously contributed their time and insights to this research. Your involvement has been instrumental in the successful completion of this thesis. In conclusion, I am deeply grateful to all those who have been part of this journey. Your support and encouragement have been a driving force behind the achievement of this milestone.

This work was supported by the National Research Facility for Lab X-ray CT (NXCT) through EPSRC grant EP/T02593X/1.

{*Blank page*}

Chapter 1

Physics Background

1.1 The Standard Model

In the field of particle physics, the Standard Model was developed as one of the most successful theoretical frameworks, that explains the interactions of fundamental particles at a subatomic scale. The Standard Model offers a comprehensive understanding of the universe at a fundamental level, it has been exceedingly effective in explaining experimental observations and of particle interactions [1]. The Standard Model includes all fundamental particle along with their antimatter counterparts. The Standard Model of elementary particles is shown in Fig. 1.1.

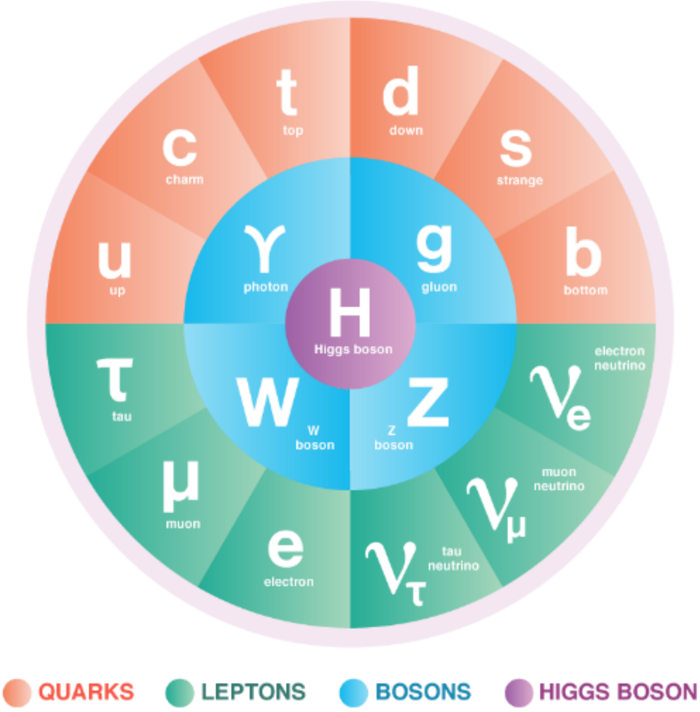

Figure 1.1: The Standard Model of elementary particles [39].

1.1.1 Fundamental Particles

The Standard Model categorises particles into two different types: fermions and bosons. All observable matter consists of fermions, divided into two categories: quarks and leptons, which form the building blocks for matter. Quarks and leptons are each associated with six distinct flavours, as depicted in Fig. 1.1. Fermions possess antimatter counterparts with identical mass and spin but opposite internal quantum numbers. Most bosons, except for the $W^+$and W^- bosons which are their own antiparticles, do not have distinct antimatter counterparts [1].

Quarks consists of up, down, strange, charm, bottom and top. These flavours possess varying mass values, as shown in Table 1.1. Baryons, such as protons and neutrons, are subatomic particles formed by the combination of three quarks. They possess an integer charge equal to the sum of the fractional charges of their constituent quarks, held together by the strong nuclear force. Mesons, a different class of subatomic particles, consist of a quark and an anti-quark pair joined by the strong nuclear force. Because of this quark-antiquark pairing, mesons have an integer electric charge. Both baryons and mesons are governed by the strong nuclear force [2].

Quark	Charge (e)	Mass
Up	+2/3	2.2 MeV/c^2
Down	-1/3	4.7 MeV/c^2
Strange	-1/3	96.0 MeV/c^2
Charm	+2/3	1.28 GeV/c^2
Bottom	-1/3	4.18 GeV/c^2
Top	+2/3	173.2 GeV/c^2

Table 1.1: Charge and mass of different flavours of quarks [2].

Along with electric charge and mass, the quarks also possess a unique property called colour charge, which describes the interaction with the strong nuclear force between quarks. Both electric and colour charge, are conserved, colour charge can be ex

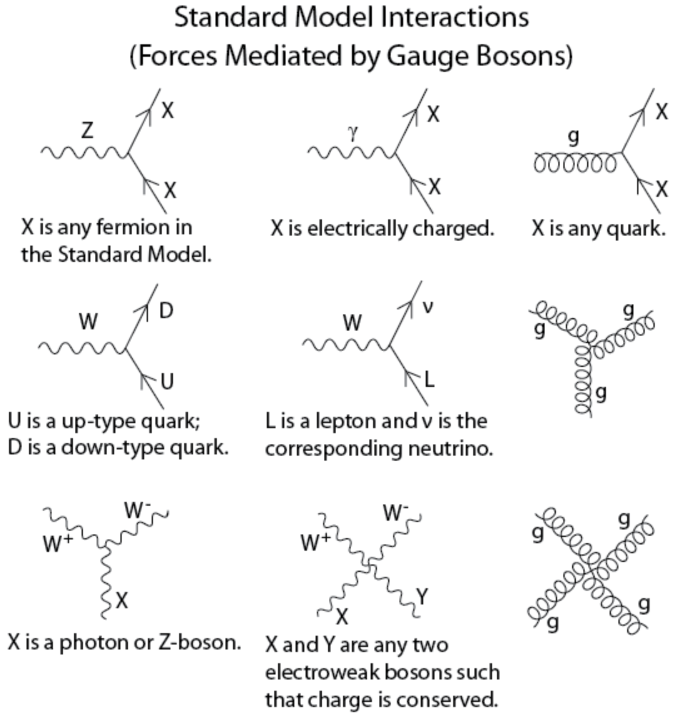

Figure 1.2: Feynman diagrams showing different Standard Model interactions [34].

changed between quarks while forming hadrons. Quark interactions are mediated via gluon, force carrying particles for the strong nuclear force. Gluons, in contrast to other bosons like photons, W, Z, and the Higgs, possess colour charge. A crucial aspect of the strong nuclear force, elucidated by Quantum Chromodynamics (QCD), is that gluons not only mediate the force between quarks but can also engage with each other. This self-interaction among gluons, along with their capacity to transport and exchange colour charge among quarks and other gluons, plays a pivotal role in governing quark behaviour and the confinement of quarks within particles like protons and neutrons [2].

The leptons are electrons, muons and taus with their corresponding neutrinos. Neutrinos have very little mass and are electrically neutral. Leptons interact with other particles using weak and electromagnetic interactions. Charged leptons primarily interact with matter using the electromagnetic force, governing their attraction and repulsion with other charged particles. Neutrinos, while electrically neutral, can interact with matter through the weak nuclear force, which is their only interaction channel. Neutrinos exhibit flavour oscillations as they traverse through matter [2].

1.1.2 Fundamental forces

Bosons are force carriers that mediate the fundamental forces between particle interactions. Bosons are of 4 types, each associated with a specific fundamental force, these include: photons, gluons, W and Z bosons and the Higgs boson. The photon is force carrier for electromagnetic interactions, it mediates interaction between charged particles. The gluons are force carriers for the strong nuclear force and are responsible for quark confinement. Gluons bind the quarks together within hadrons. The W and Z bosons are responsible for mediating weak nuclear force. The Higgs boson is part of the Higgs field and is responsible for giving parties their mass. Fig. 1.2 shows the different Standard Model interactions mediated via the gauge bosons. Bosons follow Bose-Einstein statistics, bosons have integer value of spin, due to which multiple bosons can occupy the same quantum state without any restrictions, which forms Bose-Einstein condensates, where multiple bosons have a single quantum entity at low temperatures. Unlike fermions, that follows Pauli's exclusion principle, bosons have an exchange symmetry, which allows the wave function describing the bosons to remain conserved, if the position of two identical bosons is exchanged.

The universe is governed by four fundamental forces: the strong nuclear force, the weak nuclear force, the electromagnetic force and the gravitational force. All the fundamental forces are described by the standard model, except for gravity. All the forces have different ranges over which they work and strengths. The strong and weak nuclear force dominate at very small distances (subatomic distances), while gravity and electromagnetic force have an infinite range. Gravity is the weakest force amongst the four and the strong nuclear force, as the name suggests is the strongest [2].

Three of the four (except gravity) fundamental forces are produced as a result of boson exchanges between particles. The strong nuclear force corresponds to the mediation of gluons between quarks, the weak nuclear force corresponds to the mediation of $W^{\pm}$ and Z bosons, and the mediation of photons corresponds to the electromagnetic force [2]. The graviton, a hypothetical particle, is proposed for the mediation of the gravitational force. It is a difficult challenge to integrate the gravitational force into the framework of the Standard model, as the quantum theory to describe the macro world, general relativity does not fit within the framework of the Standard model, that explains the matter interactions at the micro level. As gravity is such a weak force, its effect at the sub atomic scale is so minuscule that it can be ignored, only when there is a large amount of mass (humans, planets, etc) in consideration does the force of gravity become important.

1.1.3 Symmetries in The Standard Model

The interactions and properties of articles in the Standard Model are shaped by a foundation of various symmetries. Some key symmetries present in the model are: Gauge Symmetry, Poincaré Symmetry, Lorentz Symmetry, C-Symmetry (Charge Conjugation), P-Symmetry (Parity), T-Symmetry (Time Reversal) and Chiral Symmetry

Gauge Symmetry: The bedrock of the Standard Model's framework is established by gauge symmetry, it is responsible for the emergence of the fundamental forces and guarantees that the theory's equations remain invariant under certain transformations. Each of the different fundamental forces is linked to a specific symmetry group:

- Electromagnetic Force is governed by the U(1) gauge symmetry (Quantum Electrodynamics (QED)).
- Weak Nuclear Force is governed by SU(2) gauge symmetry (Weak Isospin).
- Strong Nuclear Force is governed by SU(3) gauge symmetry (Quantum Chromodynamics (QCD)).

Poincaré Symmetry: This symmetry encompasses translations and rotations in spacetime, ensuring the coherence of physical laws regardless of varying positions and orientations. This symmetry results in the conservation of momentum and angular momentum [3].

Lorentz Symmetry: This symmetry governs the invariance of physical laws under Lorentz transformations, which consists of boosts and rotation in spacetime. It is crucial for maintaining the consistency of the speed of light and principles of special relativity [3].

C-Symmetry (Charge Conjugation): This symmetry entails the conversion of particles into their antiparticles (or vice-versa). In the Standard Model, charge symmetry is not considered a fundamental symmetry, instead the existence of CP violation is recog nised, which is discussed in the next section. The charge symmetry alone is maximally broken in the Standard Model [4].

P-Symmetry (Parity) : Parity symmetry or P-Symmetry involves the reflecting of spatial co-ordinates (interchanging between left and right). P-symmetry was initially believed to be conserved, but with the discovery of weak interactions violating parity, the symmetry was recognised as maximally broken [4].

T-Symmetry (Time Reversal): This symmetry governs the direction of time, from negative to positive or vice-versa. In the Standard Model, although CP-symmetry is slightly broken, CPT-symmetry (combining Charge, Parity, and Time) is a perfect symmetry. The fundamental laws of physics in the Standard Model are often assumed to be T-symmetric, the behaviour of particles and their interactions can exhibit time-reversal asymmetry due to CP violation [5].

Chiral Symmetry: Chirality refers to as handedness (left or right), this symmetry relates particles of opposite chirality. This symmetry is used in the massless limit, where the particles and their mirror images counterparts behave identically [6].

The behaviour and interactions of particles within the Standard model are shaped by these fundamental symmetries. The charge, parity, time and combined symmetries are all conserved in the strong nuclear and electromagnetic forces, but these symmetries are broken in the weak nuclear force. The combined symmetry of charge and parity, CP is broken/violated under the weak nuclear force. In the Standard model CP violation has a significant effect, as it helps us understand and study the observed asymmetry between matter antimatter.

1.1.4 CP Violation

In the Standard Model Lagrangian, the Yukawa sector contains complex couplings, which were introduced to generate the masses of the fermions:

$$\mathscr{L}_{\text{Yukawa}} = -\left(\bar{U}'_L \mathbf{m} U'_R + \bar{D}'_L \tilde{\mathbf{m}} D'_R + \text{h.c.}\right)\left(1 + \frac{\Phi_o}{v}\right), \tag{1}$$

Where $U'_{L,R}$ and $D'_{L,R}$ are the 3-component vectors of the quark fields in flavour space for up and down type quarks respectively, $\mathbf{m}, \tilde{\mathbf{m}}$ are 3 x 3 matrices of complex numbers with Yukawa coupling constants ($\tilde{Y}_{ij}$ and Y_{ij}), Φ_o is the Scalar Higgs field and v is the vacuum expectation value [7].

The interactions between physical quarks coupling to neutral Z bosons preserve the observed absence of flavour changing neutral currents (FCNC). Flavour-changing neutral currents (FCNCs) describe interactions where a quark transitions between different flavours without altering its electric charge. Unlike charged current interactions mediated by $W^{\pm}$ bosons, FCNCs are forbidden at the tree level in the Standard Model. While the Z boson, as a neutral particle, can mediate interactions, it does not induce flavour changes within the Standard Model. While quark coupling with neutral Z bosons is observed with an absence of FCNCs, the coupling of physical quarks with $W^{\pm}$ bosons induce flavour mixing between different quark families. The Lagrangian for the charge-current couplings is given by:

$$\mathscr{L}_W = \frac{g}{\sqrt{2}}\left\{ \bar{U}_L \gamma^\mu W_\mu^+ \mathbf{V} D_L + \bar{D}_L \gamma^\mu W_\mu^- \mathbf{V}^\dagger U_L \right\}, \tag{2}$$

Where $\mathbf{V} \equiv V_L \tilde{V}_L^\dagger$ is a 3 x 3 unitarity matrix called the quark mixing matrix otherwise know as the Cabibbo-Kobayashi-Maskawa (CKM) matrix:

$$\mathbf{V} = \begin{bmatrix} V_{ud} & V_{us} & V_{ub} \\ V_{cd} & V_{cs} & V_{cb} \\ V_{td} & V_{ts} & V_{tb} \end{bmatrix}. \tag{3}$$

In the CKM matrix, V is the unitary matrix that describes the mixing of different generations of quarks. The implications of the CKM matrix for CP violation can be summarised in one equation based on the original quark mass matrices $\mathbf{m}, \tilde{\mathbf{m}}$:

$$\mathrm{CP} \quad \text{violation} \Longleftrightarrow \mathrm{Im}\left\{ \det\left[\mathbf{m}\mathbf{m}^{\dagger}, \tilde{\mathbf{m}}\tilde{\mathbf{m}}^{\dagger}\right] \right\} \neq 0, \tag{4}$$

From the above equation it can be inferred that, to achieve highly significant asymmetries that violate CP conservation, it is necessary to focus on highly suppressed decays, where the decay rates inherently incorporate small CKM matrix elements [7].

In the Standard Model, the charge (C) and parity (P) symmetries are drastically violated under the weak interactions of particles; however, the combined symmetry of charge and parity (CP) has been observed to have good symmetry in mostly all observed phenomena, predicted by the Standard model. The decay of B mesons is an example of phenomena that violates CP-Symmetry. CP violation has also been observed in systems consisting of bottom and charm quarks.

The CKM mechanism describes how quarks of different flavours interact and engage through the weak interactions. Within the framework of the Standard model, the violation of CP-Symmetry originates from the inherent presence of a single phase within the CKM matrix [7]. In the CKM mechanism, CP violation is crucial in explaining the matter-antimatter asymmetry in the universe. The predictions made by the Standard Model and CKM mechanism were confirmed by the experiments conducted by the BELLE and BABAR collaborations in 2001, when CP violation was observed in the decay of B mesons (mesons containing bottom/beauty quark).

CP violation arises from differences in the behaviour of certain particle processes and their corresponding antiparticles under combined parity and charge conjugation transformations. The equations that describe these processes should include complex phases for CP violation to occur. These complex phases are essential to create the conditions necessary for observing the difference in behaviours of particle and antiparticle interactions, resulting in CP violation.

Within the framework of the Standard Model, CP violation is a phenomena observed primarily at low energies, which implies that any observable impact on CP violation should diminish as the disparity in quark masses becomes insignificant [7]. Bottom and charm quark decay processes are an ideal place for detecting signals for CP violation. These decays incorporate small CKM matrix components and represent the lowest-mass interactions where all three generations of quarks play a direct role at the tree level.

1.2 Beyond the Standard Model

The Standard Model of particle physics is a well-established theoretical framework that describes particle behaviour and interactions. While it has been extremely successful at explaining various experimental observations, there are still several phenomena that the Standard model cannot account for, such as the asymmetry between matter and antimatter in the universe, Dark matter, gravity and many more. Beyond the Standard Model or BSM refers to any proposed theory or framework that goes beyond the predictions of the Standard Model. Some of the key areas of BSM research are:

Dark Matter: The Standard Model does not give any explanation for the existence of Dark matter, which is believed to make the bulk of the universe's mass. BSM theory, such as the theory of Supersymmetry, predicts the existence of new stable particles, called the Weakly Interacting Massive Particles (WIMP) that could be Dark matter candidates. Experiments at the LHC and future colliders, such as the International Linear collider (ILC) are searching for experimental proof for the existence of Dark matter [8].

Neutrino mass and oscillations: The standard Model assumes that neutrinos are massless, but experimental observations have demonstrated that they do have mass and oscillate between different flavours as they traverse through matter. Experiments, such as the NOvA (NuMI Off-Axis Electron Neutrino Appearance), T2K (Tokai to Kamioka) and DUNE (Deep Underground Neutrino Experiment) are working on improving our knowledge of neutrino masses, nature of neutrino oscillations, CP violation in neutrinos and mixing angles [8].

Quantum Gravity: The Standard Model does not include the theory of gravity within its framework. The theory of Quantum Gravity aims to reconcile the two fundamental theories of modern physics: Quantum Mechanics, which describes the behaviour of particles at a subatomic level and the theory of General Relativity, which explains the behaviour of gravity and large-scale structures in the universe. Some BSM theories that are being developed for the theory of Quantum Gravity are: String Theory, Loop Quantum Gravity (LQG), Causal Dynamical Triangulations (CDT), Asymptotic Safety and Quantum Einstein Gravity (QEG) [8].

Various BSM theories have been proposed for discovering physics beyond the Standard Model, these theories introduce new particles, new symmetries and dimensions that expand our understanding of modern physics. Experimental efforts are ongoing, including collider experiments at the LHC, as well as astrophysical observations and precision measurements are being made to test the predictions of the Standard Model and search for evidence for BSM physics.

1.3 The Large Hadron Collider (LHC)

The Large Hadron Collider (LHC) stands as the world's largest particle accelerator, measuring 27 km in circumference situated 100 m underground. Operating since 2009 at CERN (European Organisation for Nuclear Research), the LHC is designed to collide both protons and heavy ions at four different interaction points [9]. It operates based on the principles of electromagnetism and uses a combination of radio frequency cavities and superconducting magnets to accelerate particles to high energies before colliding them.

The acceleration is done in several stages, it starts with the extraction of the protons from the hydrogen source, these protons are then guided into a sequence of smaller accelerators, such as the Linear Accelerator 4 (LINAC4), where they are accelerated to an energy of 50 MeV. These protons are the injected into a sequence of circular accelerators, first the Proton Synchrotron Booster (PSB), the protons are accelerated to an energy of 1.4 GeV. Second is the Proton Synchrotron (PS), where they are accelerated to an even higher energy of 25 GeV, and finally the Super Proton Synchrotron (SPS), where they are further accelerated to an energy of 450 GeV. The protons from the SPS are injected into the LHC, where the superconducting magnets bend the proton beams to maintain circular orbit. The two beam pipes are injected with protons simultaneously under a predefined injection scheme (2808 bunches 25 nanoseconds apart with around 1×10^{11} protons in each bunch crossing) [9].

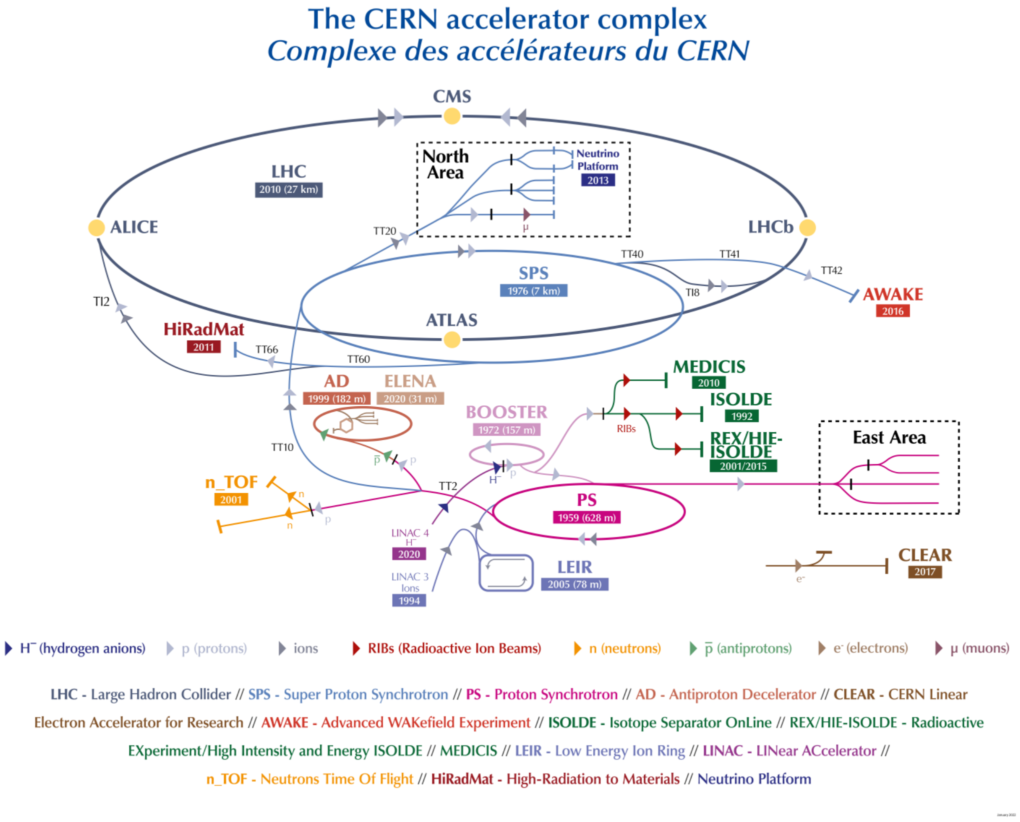

Figure 1.3: Schematic of the accelerating complex at CERN, showing the LHC along with the sequence of accelerators responsible for generating proton beams [11].

The LHC has multiple collision points where the two proton beams are brought into collision. The collision points are positioned at the intersection of the two beam lines. Focusing quadrupoles, integrated as part of the superconducting magnets, play a vital role in concentrating the beams to ensure a high probability of proton collisions. The LHC was initially designed to operate at a maximum beam energy of 7 TeV, but the energy changed after each Run (periods where the older operates at different centre of mass energies). In Run 1 (2010-2012), the centre-of-mass energy was set at 6.5 TeV. Following the Long Shutdown 1 (LS1), during Run 2 (2015-2018), the centre-of-mass energy was raised to 13 TeV. In Run 3 (since 2022), following LS2, the centre-of-mass energy has further increased to 13.6 TeV 1210. The accelerating process at the LHC is shown in Fig. 1.3 [11].

1.3.1 Experiments at the LHC

There are four main experiments at the LHC, that study a wide range of particle interaction and phenomena, aimed at deepening our knowledge about the expanding universe. These experiments are each positioned at different collision points around the accelerator ring. Each experiment possesses a distinct set of objectives and goals, collectively contributing to a comprehensive understanding of particle physics and the fundamental building blocks of the universe. All these experiments have a similar underlying structure, consisting of: Particle Identification (PID), tracking stations for reconstruction of charged particle tracks and vertices, calorimeters and muon detectors.

A Toroidal LHC ApparatuS (ATLAS): The ATLAS is the largest experiment at the LHC. The experiment equipped with a general-purpose detector, which is used to study the high transverse momentum interactions at the LHC. Together with CMS, the two collaborations were responsible for the discovery of the Higgs Boson in 2012. The experiment is designed to study wide range of fundamental physics phenomena, such as: studying the properties of the Higgs Boson, examining the behaviour of quarks and gluons in proton-proton collisions and taking precision measurements of known particles, such as the $W^{\pm}$and Z bosons. The ATLAS detector is equipped with various sub-detectors, such as tracking chambers, calorimeters and muon detectors, to detect and analyse particles produced during high energy collisions. Fig 1.4 shows the cross-section of the ATLAS detector [12].

Compact Muon Solenoid (CMS): The CMS, similar to ATLAS, has another general purpose detector. CMS contributed significantly to the discovery of the Higgs Boson. The CMS experiment was designed to study the properties of the Higgs Boson, study the properties of heavy quarks and leptons and search for new physics beyond the Standard model. Similar to the ATLAS collaboration, CMS also aims to make precision measurements of known particles and their interactions [13]. The cross-section for the CMS detector can be seen in Fig. 1.5.

A Large Ion Collider Experiment (ALICE): The ALICE experiment is designed to study he behaviour of particles, especially heavy ions under extremely high energy densities and temperatures, similar to the conditions that existed shortly after the Big Bang. The collaboration primarily uses lead ion collisions to conduct these studies. In addition to heavy-ion collisions, the collaboration also concentrates on the study of quark-gluon plasma. ALICE also works on production and analysis of rare particles, produced during heavy-ion collision [14]. The cross-section for the ALICE detector can be seen in Fig. 1.6.

Large Hadron Collider Beauty (LHCb): The LHCb experiment is designed to study the properties of the beauty/bottom quarks. The experiment focuses on the study CP violation in the decays of B mesons and rare decays, it aims to investigate and explain the matter antimatter asymmetry in the universe by studying decays of B and C quarks. In addition to studying the decays of B mesons, the collaboration uses the data from

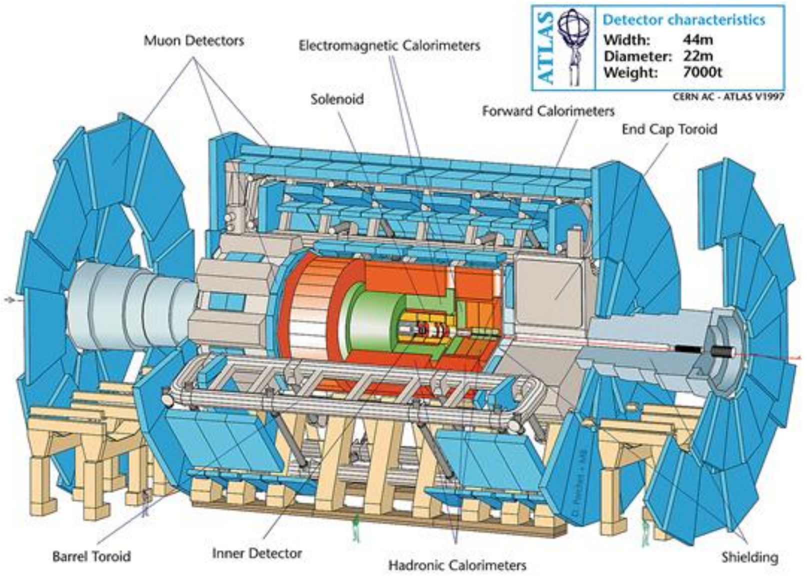

Figure 1.4: Schematic overview of the ATLAS experiment [30].

these decays to test the predictions made by the CKM mechanism. In addition to its primary physics goals, the collaboration also places significant emphasis on studies related to forward physics, lepton universality, beyond the Standard Model (BSM) physics, hadron spectroscopy, and rare decays [15]. The detector cross-section for the LHCb and LHCC experiment is shown in Fig. 1.7.

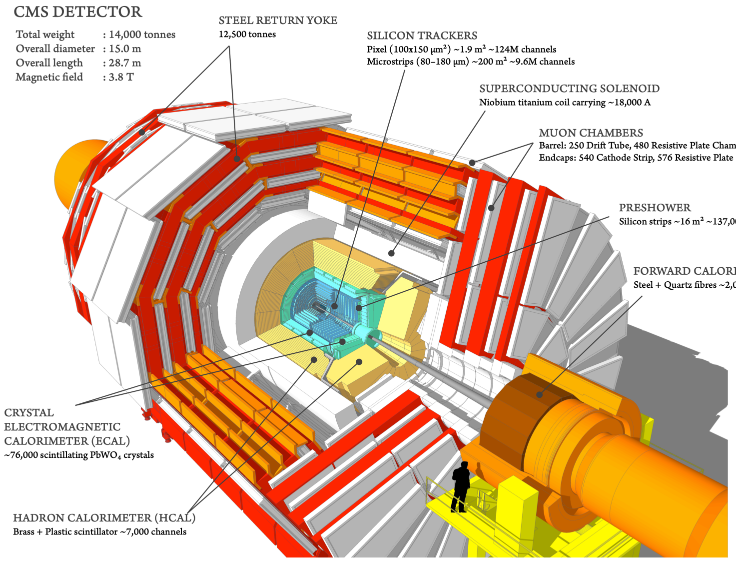

Figure 1.5: Schematic overview of the CMS experiment [31].

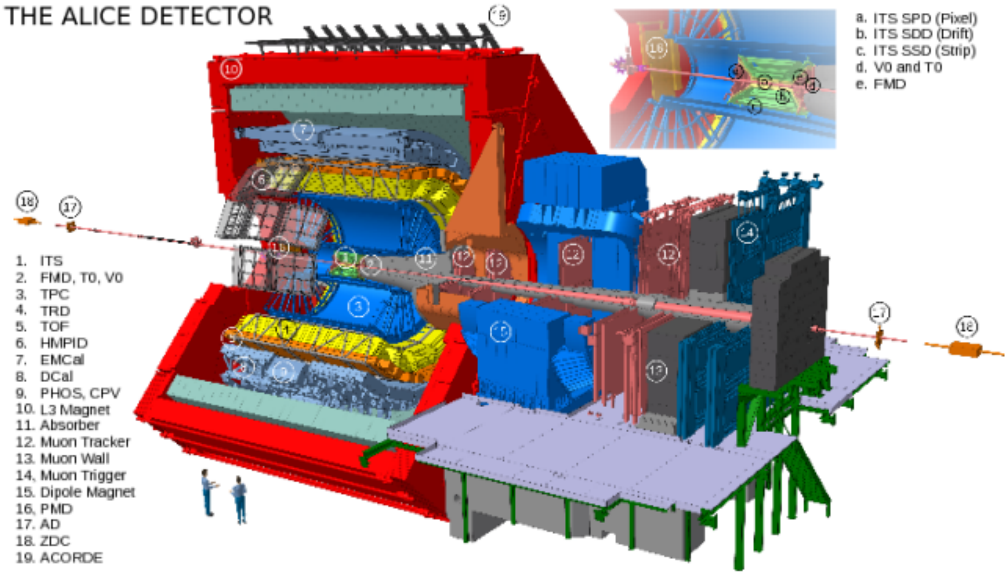

Figure 1.6: Schematic overview of the ALICE experiment [32].

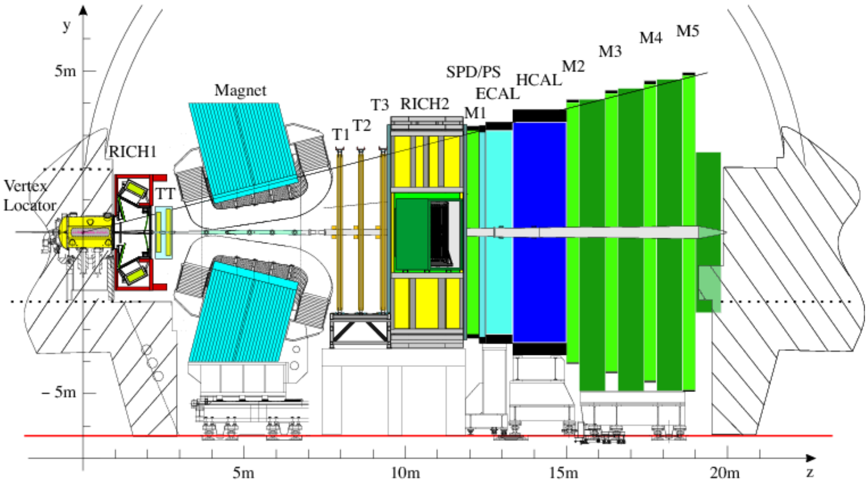

Figure 1.7: Schematic overview of the LHCb experiment [15].

1.3.2 LHCb

The LHCb detector is a complex apparatus that encompasses several tracking stations and sub-detectors, each of which serve a specific purpose in detecting and measuring different properties of the particles produced in the high energy collision. The detector's main focus is to investigate the nature of CP violation in heavy quark flavours, such as the beauty/bottom and charm quarks. To extract interesting events from a data set with a large background, the detector system must have an excellent Particle identification (PID) and tracking systems [15].

During Run 2 of the Large Hadron Collider (LHC) data collection period (2015-2018), the detector operated at a peak luminosity of 4×10^{32} cm^{-2} s^{-2}. This value falls below the LHC's maximum achievable luminosity (1×10^{34} cm^{-2} s^{-2}). While lower luminosity equates to a lower particle density, it offers several advantages for the detector's research objectives. Reduced background noise allows for more precise measurements. Additionally, a lower particle density minimises pile-up (multiple proton-proton collisions within a single bunch crossing), thus improving trigger efficiency. Conversely, higher peak luminosities would lead to a significant increase in background events, hindering the researchers' ability to isolate events of interest. Consequently, operating at a lower luminosity allows the researchers to focus on a smaller dataset of high-quality events, simplifying data analysis. The detector is a single arm forward spectrometer, designed to investigate the heavy quarks flavours in the pseudorapidity (η) (angular distribution of particles produced in high energy collisions) range of $2 < \eta < 5$. Pseudorapidity (η) remains invariant under Lorentz transformations, as a result pseudorapidity becomes a useful variable used for describing the angular distribution of particles. The decay products from the decay of beauty/bottom and charm quarks have a large forward momentum, resulting in the majority of the final state particles being produced in the forward region. Precision measurements of the quark (beauty/bottom and charm) decays can be made by focusing in this specific bandwidth of pseudorapidity. Hence, despite encompassing only 2.3% of the solid angle, 24% of all $b\tilde{b}$ quark pairs are produced in the LHCb acceptance range, at a centre-of-mass energy of 14 TeV, that are contained in the whole acceptance region [16], [17].

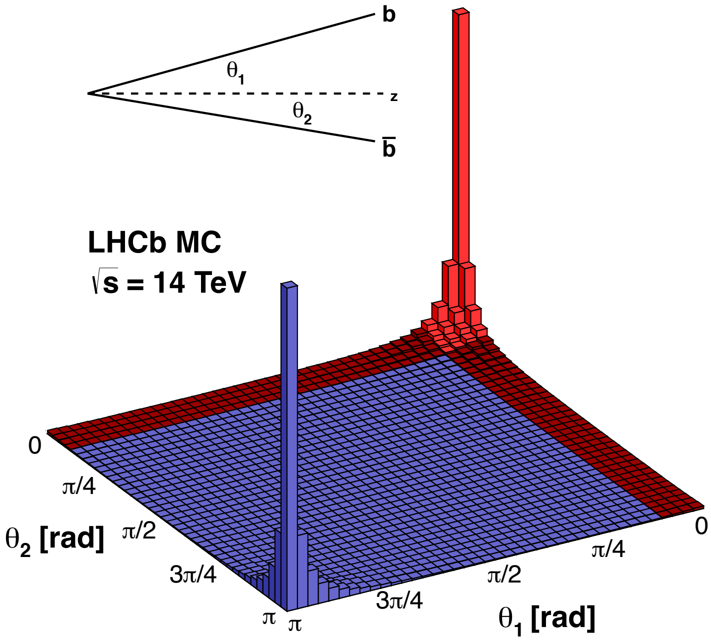

Figure 1.8: Angular distribution of $b\tilde{b}$ quark pairs produced at a centre-of-mass energy of 14 TeV. The red region displays the LHCb acceptance region [16].

The LHCb coordinate system is defined by the Cartesian coordinate system, the z- axis is defined along the beam line, pointing in the direction of the particle beam passing through the detector. The y-axis is perpendicular to the beam line and points upwards, with an acceptance of ±250 mrad and the x-axis is defined along the horizontal direction, pointing towards the centre of the LHCb detector, with an acceptance rate of ± 300 mrad .

In the LHCb, as part of Upgrade 2 these subsystems are implemented as: VELO, RICH 1, SciFi, RICH 2, Electromagnetic Calorimeter (ECAL), Hadronic Calorimeter (HCAL) and Muon Chambers. These systems will be discussed in detail in Chapter 2.

{Blank Page}

Chapter 2

The LHCb Detector

The LHCb experiment was originally designed for the study of CP violation Andrade decays of heavy flavour hadrons. However, its versatile detector has facilitated research in additional areas including Electroweak Physics, Heavy Ion Physics, Fixed Target Physics, Forward Region Physics (study of particle interactions at very small angles and high rapidities), and Beyond Standard Model Physics. Operating from 2010 to 2018 during LHC Run 1 (2010-2012) and Run 2 (2015-2018), the LHCb experiment collected a comprehensive dataset, including 9 fb^{-1} in proton-proton collisions, 30 nb^{-1} in proton-lead and lead-lead collisions, and 200 nb^{-1} in fixed target collisions. Despite the substantial data acquired during these runs, the precision of key flavour physics observables studied by LHCb remains constrained by its integrated luminosity and statical limitations posed by the Level 0 hardware trigger. The solution to address these limitations came in the form of the LHCb Upgrade 1. This upgrade has been specifically designed to operate at a nominal instantaneous luminosity of 2×10^{33} cm^{-2} s^{-1}, with a corresponding crossing rate of 30 MHz [18].

The current LHCb detector, as part of Upgrade 1 has the SciFi (Scintillating Fibre) tracker, which replaces the previous Inner and Outer Tracking systems, the Upstream Tracker (UT), which replaces the Tracker Turicensis (TT), VELO (Vertex Locator), RICH, calorimeters and Muon chambers. The events are reconstructed and selected by an entirely software-based trigger system, which performs real-time event reconstruction at the visible interaction rate of approximately 30 MHz. As part of Upgrade 1, the trigger efficiency will be improved by a factor of two for nearly all decay modes. This enhancement is anticipated to result in annual yields from most channels that are an order of magnitude greater than those achieved in the previous experiment [19]. These enhancements in luminosity and trigger efficiency are expected to enable more precise measurements of heavy flavour interactions and facilitate the discovery of new physics. With the development of the HL-LHC (High Luminosity Large Hadron Collider), the

LHCb collaboration has proposed the Upgrade 2 to the LHCb detector, which is to be installed during LS4 (Long Shutdown 4) and is expected to be taking data by 2034 during Run 5. The upgrade is estimated to operate at luminosities of around 1.5×10^{34} cm^{-2} s^{-1}. The upgrade will enable data collection at a minimum of 300 fb^{-1} allowing for precise measurements of many observables that are beyond the capabilities of current detectors [20]. With this upgrade, several detector enhancements and additions are foreseen to be implemented across various components of the experiment. These include upgrades to the VELO (Vertex Locator), the introduction of HV-MAPS (High Voltage-Monolithic Active Pixel Sensors) in the Upstream Tracker, enhancements to the SciFi trackers with the introduction of the Mighty Tracker (Hybrid detector combining inner pixel and outer SciFi tracker for optimal precision in particle tracking), improvements in Particle Identification (PID) detectors like RICH (Ring Imaging Cherenkov) and the addition of a new detector called TORCH (Time of internally Reflected Cherenkov Light) [19]. Additionally, upgrades are planned for the ECAL (Electromagnetic Calorimeter) and Muon Chambers. A side view of the proposed detector is shown in Fig. 2.1.

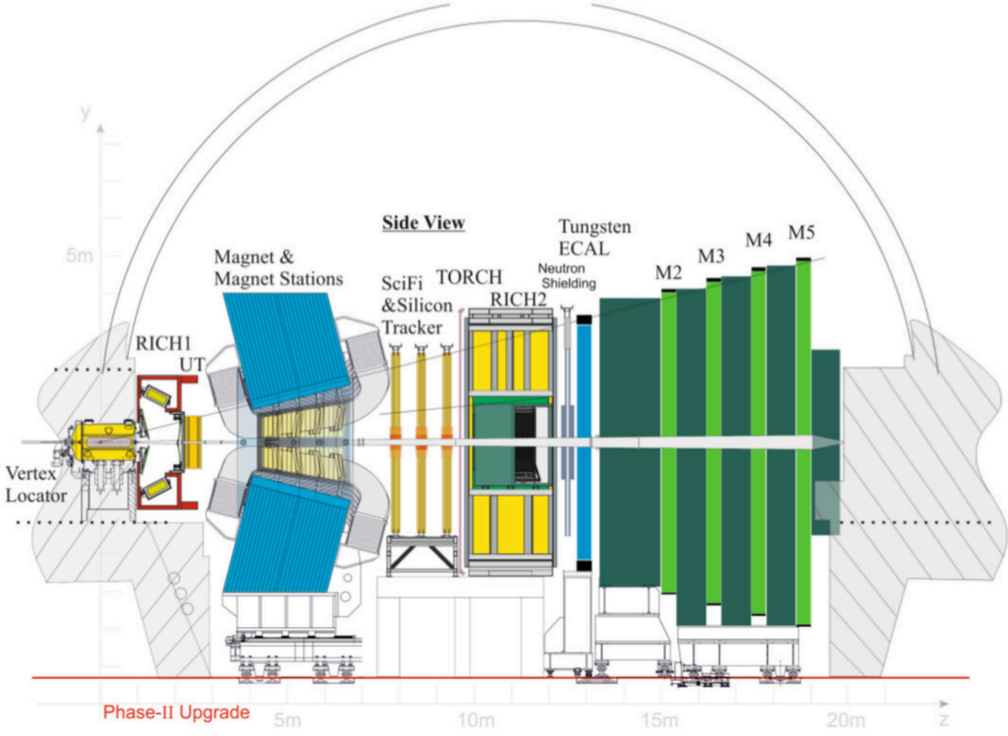

Figure 2.1: Side view of the Upgrade 2 detector at the LHCb [19].

2.1 LHCb Upgrade 1

To cope with the challenges of ever-increasing data rates and radiation exposure, LHCb Upgrade 1 has transitioned to a completely software-triggered experiment. This necessitates a substantial overhaul of the hardware systems. The new tracking systems utilise the familiar x-u-v-x pattern with a 5° interval between each system, as shown in Fig. 2.2.

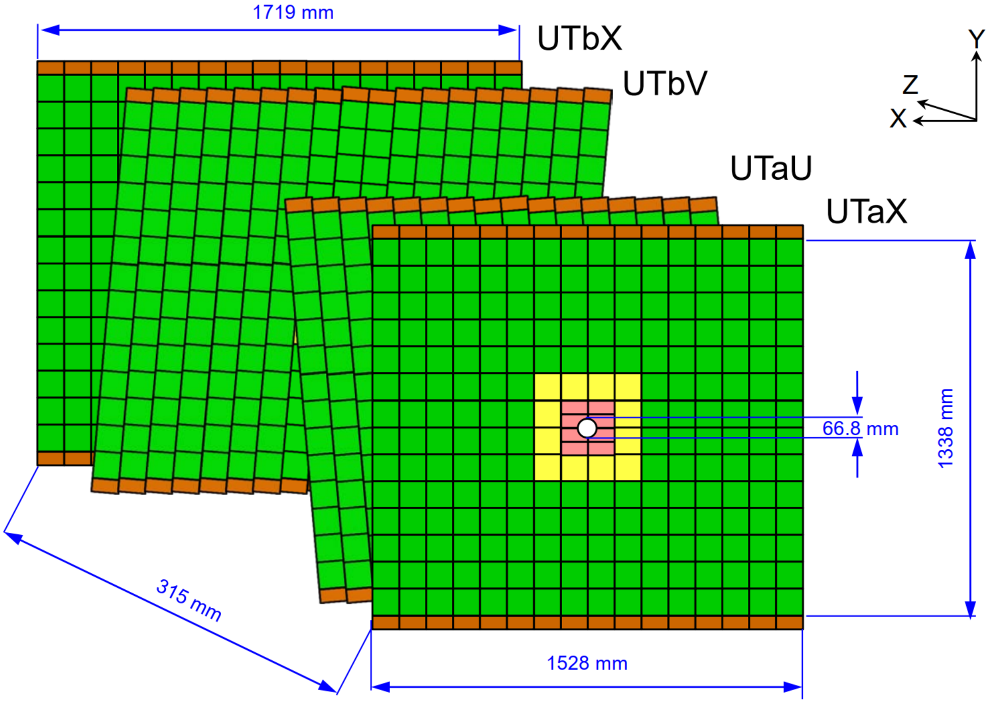

Figure 2.2: Schematic showing the sensor layout and dimension in each region of the UT [18].

Scintillating Fibre Tracker (SciFi): The SciFI tracker is developed using scintillating fibres, which are 250 μm thick, flexible plastic fibres that emit light when a charged particles passes through them. This tracker is used to detect the paths of charged particles, the light emitted by these particles is collected and the data is then used to reconstruct the trajectories of the particles. The SciFi tracker is intended to improve the tracking capabilities of the LHCb detector, enabling better reconstruction of particle paths and more precise measurements of particle properties. This tracker replaces the previous Inner and Outer trackers (IT and OT) in the LHCb detector [18].

Upstream Tracker (UT): The Upstream Tracker is developed using silicon strip technology. Similar to the SciFi tracker, the UT is designed for particle tracking and secondary vertex reconstruction. The UT is positioned close to the collision point, upstream from other detectors in the experiment. Because of its proximity to the collision point, the detector is exposed to a high detector flux, enabling effective management of high track multiplicity, which, in turn, enhances particle reconstruction. The tracker is designed to replace the Tracker Turicensis (TT) [18]. Along with tracks reconstruction, the UT also provides precise measurements of the particles momentum by measuring the particles position along their curved path at multiple intervals. The sensor type, dimensions and layout in each region of the UT are shown in Fig. 2.2.

2.1.1 Vertex Locator

The Vertex Locator (VELO) detector is a critical component of the LHCb experiment. The sub-detector is specifically designed to precisely measure the trajectories and position soft particles produced during the high-energy proton-proton collision. For accurate and efficient track reconstruction, the VELO is placed closest to the point of collision, with modules placed on either side of the beam pipe. Along with track reconstruction, the detector is also used in distinguishing tracks originating from long and short lived decay of particles [18].

The impact parameter resolution (σ_{IP}^2) is a key metric in the design of the vertex detector. It represents the precision with which the perpendicular distance to a track is measured, with respect to a fixed point. In the case of the VELO, this metric can be approximated as follows, [18]

$$\sigma_{\mathrm{IP}}^2 \approx \underbrace{\left(\frac{r_1}{p_{\mathrm{T}}[\mathrm{GeV}/c]}\right)^2 \left(0.0136\mathrm{GeV}/c\sqrt{\frac{x}{X_0}}\left(1+0.038\ln\frac{x}{X_0}\right)\right)^2}_{\text{multiple scattering}} + \underbrace{\frac{\Delta_2^2\sigma_1^2+\Delta_1^2\sigma_2^2}{\Delta_{12}^2}}_{\text{extrapolation}} \quad (5)$$

Here, the equation describes the metric as a function of, the track's transverse momentum p_T, the distance between the first and second measurements Δ_i $(i = 1{,}2)$, the positional uncertainties associated with those measurements σ_i, and the average axial distance of the material encountered before the second measurement r_1. The constant x/X_0 describes the fraction of radiation length traversed before the second measurement. The multiple scattering term in Eq. (5) accounts for the degradation caused by multiple scattering events, while the extrapolation term addresses the error introduced by the detector's geometry, including factors such as the lever arm and pixel size. As the impact parameter resolution serves as the performance metric for the VELO, enhancing performance involves reducing the radial distance to the beam axis of the first pixel hits [18]. However, this adjustment must be carefully balanced with the

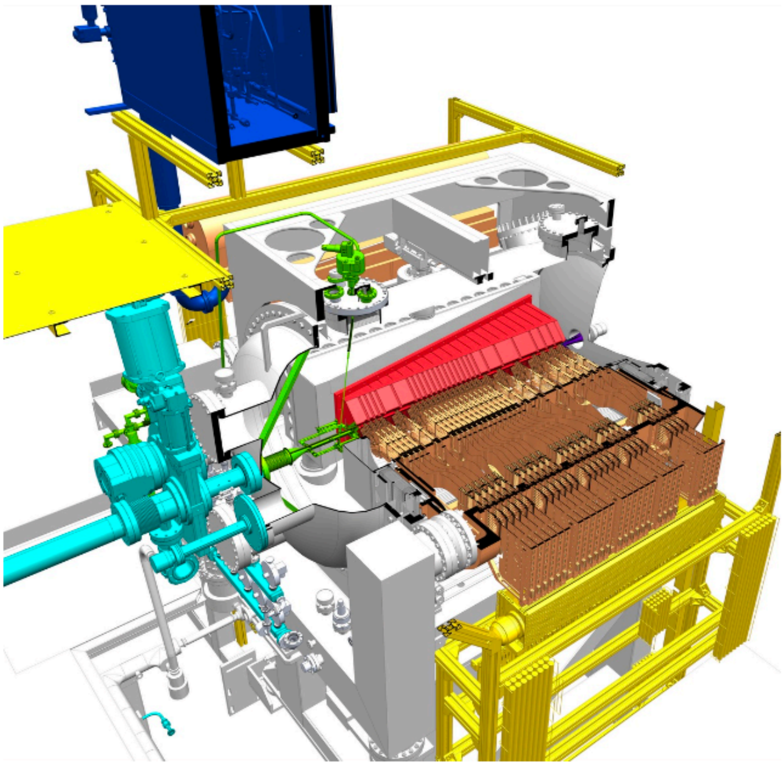

Figure 2.3: This 3D view showcases the upgraded VELO detector with a cut-out section revealing several key components associated with the upgrade. These include the brown coloured Side C pixel modules and their associated readout electronics. The red coloured Side A RF box is also visible. The green volume represents the internal gas target system, including its storage cell. Finally, the cyan coloured section highlights the upstream beam pipe and the sector valve. [18].

constraints posed by the proximity to the beam-line. The minimal VELO aperture, as mandated by LHC collimation and protection requirements, is contingent on several factors, including the beam direction concerning the longitudinal axis of the VELO (crossing angle), the maximum anticipated separation of counter-rotating beams, the transverse size of these counter-rotating beams, and the mechanical stability and precision of the RF (radio frequency) boxes. Considering all the requirements and relevant factors, a radial clearance of 3.5 mm is chosen for the RF boxes, allowing the closest active pixel edge of the silicon sensors to be positioned 5.1 mm away from the beam line [21].The VELO detector is constructed around the primary vacuum beam pipe, with various components such as sensor modules, support structures, cooling systems, and readout electronics enclosed within a secondary vacuum environment. The RF boxes utilised for the detector are designed to be leak-tight and can withstand a pressure difference of up to 10 mbar between the two vacuums. The components inside the secondary vacuum, including sensor modules, support structures, cooling systems, and readout electronics, are fabricated from materials with minimal outgassing properties. This secondary vacuum environment serves to minimise interactions with atmospheric gases and other particles, preserving particle tracks and prevents contamination from atmospheric dust, thereby preservingCO_2 the detector's performance. The VELO employs a bi-phase cooling system to maintain the detector's temperature. CO_2 circulates through microchannels etched into the silicon cooler, which serves as the platform for attaching all active detector components. The operational temperature for the FE ASIC sensors must remain below -20°C, even during periods when the detector is not in use, such as shutdown periods. The schematic cross-section of the VELO is shown in Fig. 2.3 [18].

2.1.2 RICH

The Ring Imaging Cherenkov (RICH) detector is developed for identifying charged particles, particularly pions, kaons and protons, based on the Cherenkov radiation they emit when moving through a medium at a speed greater than the speed of light in that medium. The detectors primary aim is separate pions and kaons, and measure their momenta [18]. The detector uses Cherenkov Radiation to determine the velocity and mass of the emitted particle. The angle of the emitted Cherenkov cone of light depends

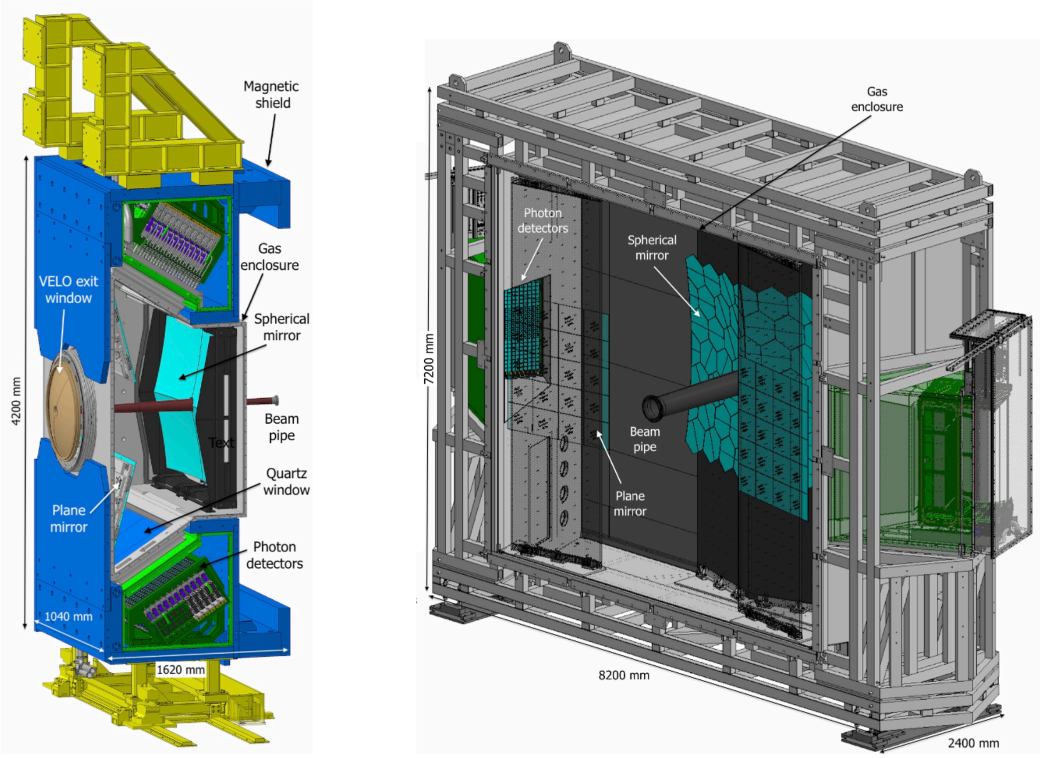

Figure 2.4: Schematic overview of the RICH1 (left) and RICH2 (right) detectors [18].

on the particle's velocity, which is directly related to its mass and energy. By measuring the angle of the emitted Cherenkov light and using the momentum measurement of the tracking detectors, the detector can infer the particle's identity.

The detector consists of an optical system that collects and focuses the light produced by the charged particles undergoing Cherenkov Radiation (Cherenkov light). The Cherenkov light is then detected by an array of photodetectors, such as multi-anode Photomultiplier tubes (MaPMTs). These detectors capture the Cherenkov light and convert it into electrical signals. The RICH system is designed as a two part system with RICH1 positioned upstream from the magnet and RICH2 placed downstream from the magnet. Both the RICH1 and RICH2 detectors have the same construction, but differ in the mode of detection. Both detectors use multi-anode photomultiplier tubes (MaPMTs) to detect the Cherenkov light from emitted from incoming particles [18]. The cross-section schematic of both detectors is shown in Fig. 2.4.

The RICH1 uses C_4F_{10} (perfluorobutane) as its radiator gas. Perfluorobutane has a relatively low refractive index as compared to air, which implies that only particles with a higher velocity will be able to produce Cherenkov radiation, hence making the Particle Identification (PID) process much more efficient. On the other hand RICH2 uses CF_4 (carbon tetrafluoride) as its radiator gas, which as higher refractive index than air. As RICH1 is used for identifying particles with high velocities, the RICH2 detector is used to identify particles with lower velocities (Cherenkov radiation is only produced by charged particles travelling faster than a specific threshold velocity, which is greater than the speed of light in the medium but slower than the speed of light in a vacuum), such as electrons. Combined, the two detectors can identify a wide range of particle produced in the high energy proton-proton collision. The RICH optimal performance requires track polar angles between 90-180 mrad for RICH1 and 40-90 mrad for RICH2 [18].

2.1.3 Calorimeters

The Calorimeters used in the LHCb are designed to measure the energy of particles produced during the high-energy proton-proton collision. These detectors are essential for Particle Identification (PID) and are particularity effective in identifying neutral particles, such as photons or neutral hadrons. When charged or neutral particles interact with the material of the calorimeter, electromagnetic or hadronic showers are produced, depending on the particle type and energy. These showers of secondary particles then interact with scintillators. The light produced in the scintillator is then transferred to Photo Multiplier Tubes (PMTs), which convert the light signal to an electrical signal.

Electromagnetic showers are produced when particles, such as electrons and photons interact with the calorimeter material, undergo pair production, Compton Scattering and bremsstrahlung, generating secondary particles that deposit their energy into the calorimeter. Hadronic showers, initiated by both neutral (e.g., neutrons, neutral pions) and charged hadrons (e.g., protons, charged pions), differ from electromagnetic showers. In these showers, neutral and charged hadrons interact with the calorimeter, generating secondary particles through hadronic interactions. Subsequently, these secondary particles deposit their energy into the calorimeter.

The Calorimeters at LHCb are divided into different layers/sections. These sections are designed to absorb and measure the energy of particles with varying properties and energy ranges. Different materials, such as lead or tungsten, are used in the construction of calorimeter layers to optimise energy measurement for specific particle types.

Electromagnetic Calorimeter (ECAL): The ECAL is designed to absorb and measure the energy of electromagnetic showers, produced by particles, such as electrons and photons. The detector is made from a combination of 2 mm lead, 4 mm scintillating tiles and 120 μm of Tyvek (flash spun high-density polyethylene fibres, used to enhance efficiency of light reflection) layers, stacked on top of each other [18]. The schematic cross-section of the ECAL cell is shown in Fig. 2.5.

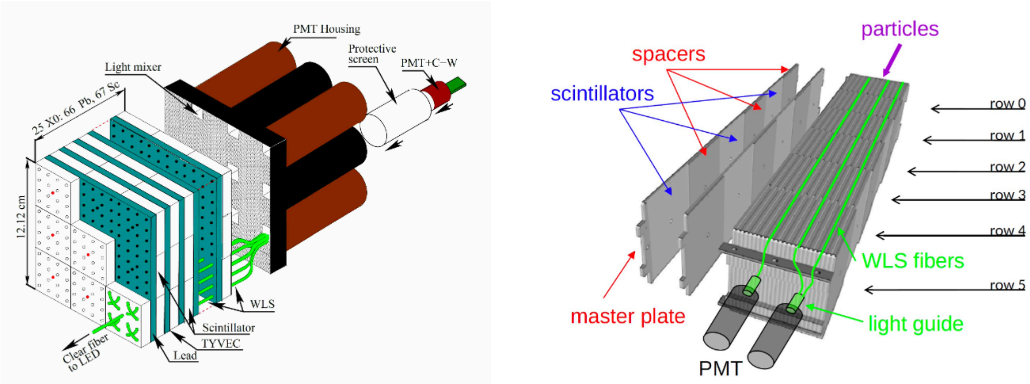

Figure 2.5: Schematic cross-section of the ECAL (left) and HCAL (right) cells [18].

Hadronic Calorimeter (HCAL): The HCAL is designed to measure the energy produced by hadronic showers. The detector is used for Particle Identification (PID), event reconstruction, neutral hadron detection, jet reconstruction and background rejection (signals that mimc particle signals). The HCAL consist of detector plates placed parallel to the beam pipe. These plates are made from alternating tiles of iron and scintillators placed every 20 cm [18]. The schematic cross-section of the HCAL cell is shown in Fig. 2.5.

2.1.4 Muon Chambers

The Muon Chambers are an array of detectors designed to identify and measure the trajectories of muons. These detectors are positioned at the end of the LHCb experiment, farthest point from the primary vertices. The Chambers consists of 4 stations from M2 to M5. The M2 to M5 stations are positioned downstream from the calorimeters. The four downstream stations are equipped with multi-wire proportional chambers (MWPC) and 80 cm thick iron absorbers to filter out low-energy particles. Each MWPC comprises four independent layers, each featuring anode wires positioned between two cathode planes, ensuring both high redundancy and efficiency. Originally, a fifth station (M1) was located upstream of the calorimeters, consisting of 12 gas electron multiplier (GEM) detectors in the innermost region and 264 MWPCs. The M1 station was employed in the Level-0 (L0) hardware trigger but is no longer required as part of the upgraded system [18].

Muon Chambers are based on gas detectors, where the detectors use a gas-filled volume as a medium through which the muons travel, as the muons travel through the gas, they ionise the gas molecules around them, creating Ionisation electrons. These ionised electrons drift towards anode strips placed in the chamber. The ionised electrons produce an electrical signal as they drive towards the anode strip, this signal is then amplified to produce measurable electronic signals. The position of the muon's trajectory can then be reconstructed with high precision, by analysing the electric signals from multiple anode strips. The detectors help with background rejection by accurately distinguishing genuine muons from signals mimicking muons based on precise trajectory measurements from the Muon Chambers [18].

2.1.5 Software Trigger and DAQ

LHCb uses the TELL40s (Trigger and Event Link for LHCb at 40 MHz) for Data Acquisition (DAQ) from front end chips of all the sub detectors in the experiment [22]. The TELL40s system is designed to handle data flow between the detectors, trigger system and data acquisition infrastructure. The system receives trigger decisions from different stages of the trigger system (HLT1 And HLT2) and forwards these decisions to relevant detector components for event selection. System also ensures that the data from sub-detectors and trigger stages are synchronised correctly, to maintain proper chronological order of events. The TELL40s uses Field-Programmable Gate Array (FPGA) cards, working on a PCIe 4.0 (Peripheral Component Interconnect Express 4.0) interface to perform data formatting and packaging to prepare the data for transmission to the DAQ systems [23].

The LHCb initially used a hardware trigger to reduce the rate for the readout system, with the increased luminosity of the LHC, clocking in at 40MHz, with a bunch crossing every 25 nanoseconds [23]. Hardware triggers use a set of predefined selection criteria to quickly identify events of potential interest to the experiment. These triggers are implemented as a series of layers, each responsible for detecting specific features of the collision event. Events are filtered out through the layers that do not meet the selection criteria. The predefined section criteria allow the triggers to extract relevant information, such as energy deposits or particle trajectories. The primary purpose of the hardware trigger is to reduce the size of data coming in from the collision, to a more manageable size. Hardware triggers efficiently reduce data volume but may overlook rare and complex particle interactions due to predefined selection criteria that may not cover the full range of unexpected or uncommon events. They also tend to reject common low energy signatures[18].

With the LHCb upgrade, the collaborations has changed to using a software trigger, that offer greater flexibility and analysis capabilities. Unlike hardware triggers, software triggers use complex algorithms to analyse data from multiple detector components and make informed selections based on a wide range of physics criteria. These triggers extract features from the data collected from detectors and apply the predefined physics criteria in real-time. The analysis implements intricate pattern recognition, statistical analysis, and comparisons against expected behaviours for different physics processes. The trigger is able to evaluate multiple criteria simultaneously, which allows it to capture a wide range of particle interactions, including rare decays of b- and c- mesons. One significant advantage the software triggers have over the hardware triggers is the high level of adaptability that they provide. The event selection criteria can be modified and fine-tuned based on new discoveries.

The trigger system at the LHCb is split into two main stages: Hight Level Trigger 1 (HLT1) and High Level Trigger 2 (HLT2).

High-Level Trigger 1 (HLT1): The HLT1 is the first stage of the LHCb software trigger system. The HLT1 uses complex algorithms to extract features from the preprocessed data set, such as track reconstruction, PID, invariant mass calculations, impact parameters, particle energies, pattern recognition and event topology analysis. The HLT1 aims to capture broader range of physics phenomena by reconstructing particle tracks, identifying particle types, and performing preliminary analyses [18].

High-Level Trigger 2 (HLT2): The HLT2 is the final stage of the LHCb trigger system before data recording. The HLT2 performs advanced analysis, such as rare process identification, multivariate analysis, particle reconstruction, secondary vertex identification and Invariant mass calculations on the preprocessed data set to make an informed decisions about event selection. The HLT2 mainly focuses on rare decays of b- and c-mesons. The events recorded by HLT2 are passed on for further offline analysis [18].

The online buffer stores events from HLT1 while real-time alignment and calibrations are being conducted. Additionally, it enables events selected by HLT1 to be buffered for processing between LHC fills, effectively enhancing the processing capacity for the HLT2 computing resources [18]. Fig. 2.6 shows a flowchart for the software trigger system at the LHCb.

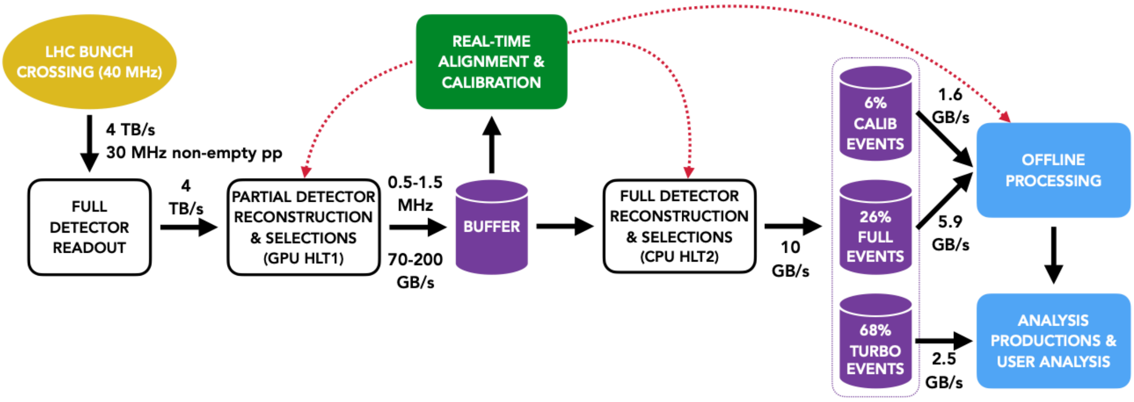

Figure 2.6: Software trigger topology for LHCb [18].

2.2 The Mighty Tracker

As part of the LHCb upgrade 2 the inner modules of the SciFI detector are considered to be replaced during LS4 due radiation damage. With this upgrade the LHCb will be operating at an increased Luminosity of 2×10^{34} cm^{-2}s^{-1} during Run 5 and Run 6. As a result of the increased luminosity, the SciFi fibres will experience a higher occupancy. This will lead to an increased rate of fake tracks due to the absence of y-axis segmentation, which limits the detector's ability to differentiate tracks originating from the same spatial location along the beam axis. The increased radiation environment will cause faster radiation damage, resulting in a shorter attenuation length of the SciFi fibres, which will in turn lead to less light being measured at the SiPM (Silicon Photomultipliers), negatively impacting the tracking performance. To prevent this decline in tracking performance, a silicon pixel tracker can be placed in the region of highest occupancy (central region of the detector with the highest radiation damage). The addition of the central silicon tracker would result in a hybrid detector, comprising both Scintillating fibre and silicon pixel detectors. This hybrid detector would provide fine granularity, reduced ghost rates and high radiation tolerance in the inner regions. Meanwhile, the outer regions would benefit from the lower-material fibre components [23]. The Upgrade 2 timeline can be seen in Fig. 2.7.

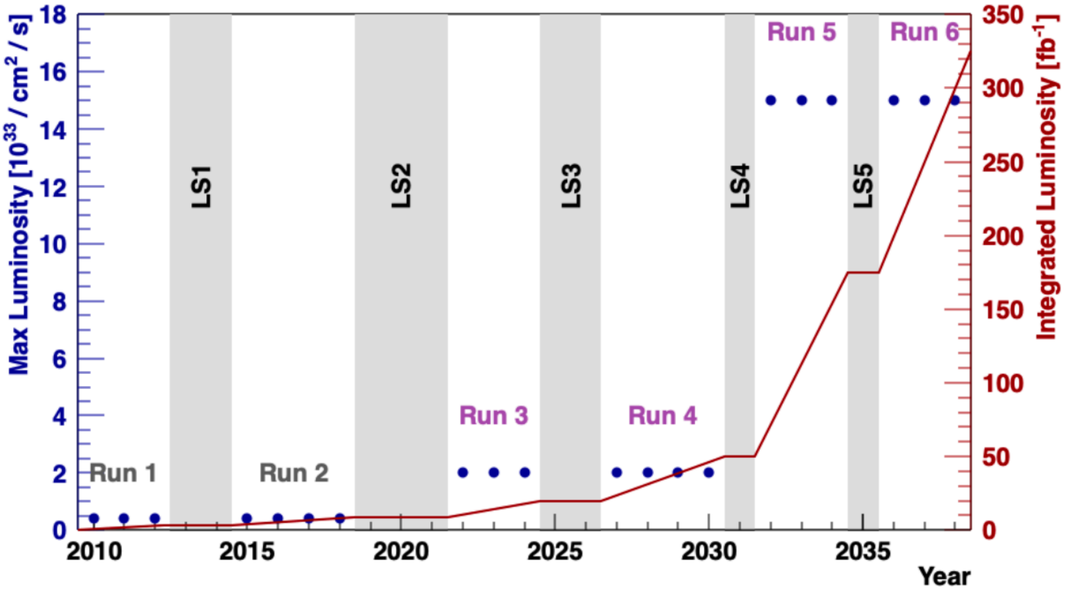

Figure 2.7: Timeline for the LHCb Upgrades 1&2 (Run 3 to Run 6) [19].

The silicon pixel trackers are foreseen to be outfitted with High Voltage Monolithic Active Pixel Sensor (HV-MAPS) pixels, based on Complementary Metal-Oxide-Semiconductor (HV-CMOS) technology. These sensors have excellent spatial resolution, fine segmentation and high granularity with a pixel size of 50 µm 150 µm , which is crucial for precise tracking measurements. The sensors also have integrated readout electronics, enabling fast data readout. The HV-MAPS sensors operate effectively in the harsh radiation environment of LHCb, demonstrating good performance up to 3×10^{16} 1 MeV $\mathrm{n}_{eq}/\mathrm{cm}^2$ fluence levels [19].

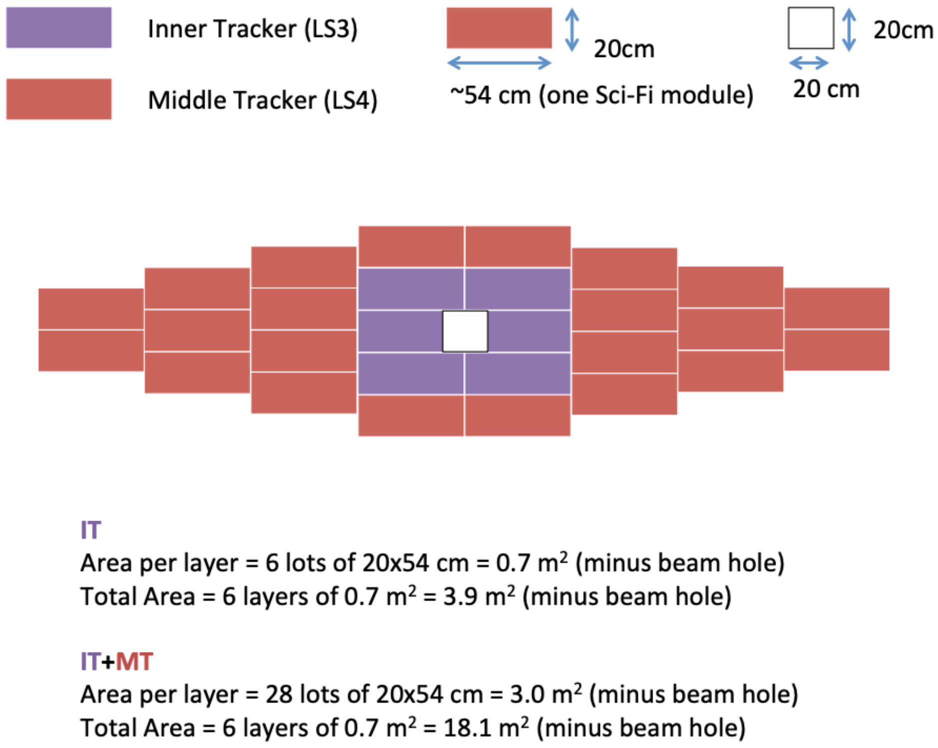

IT
Area per layer = 6 lots of 20x54 cm = 0.7 m^2 (minus beam hole)
Total Area = 6 layers of 0.7 m^2 = 3.9 m^2 (minus beam hole)

IT+MT
Area per layer = 28 lots of 20x54 cm = 3.0 m^2 (minus beam hole)
Total Area = 6 layers of 0.7 m^2 = 18.1 m^2 (minus beam hole)

Figure 2.8: Schematic illustration of the Mighty Tracker’s, Inner and Middle Tracker [23].

The Inner Tracker (IT) corresponds to the purple region shown in Fig. 2.8 and the Middle Tracker (MT) corresponds to the red region, planned to be installed during LS4. Both IT and MT modules have the same horizontal dimensions as one SciFi module. The dimensions of the IT and MT are determined by factors such as radiation damage to the SciFi fibres, considerations of occupancy, and track reconstruction performance under Upgrade II conditions. The Mighty Tracker will be formed by the outer scintillat-

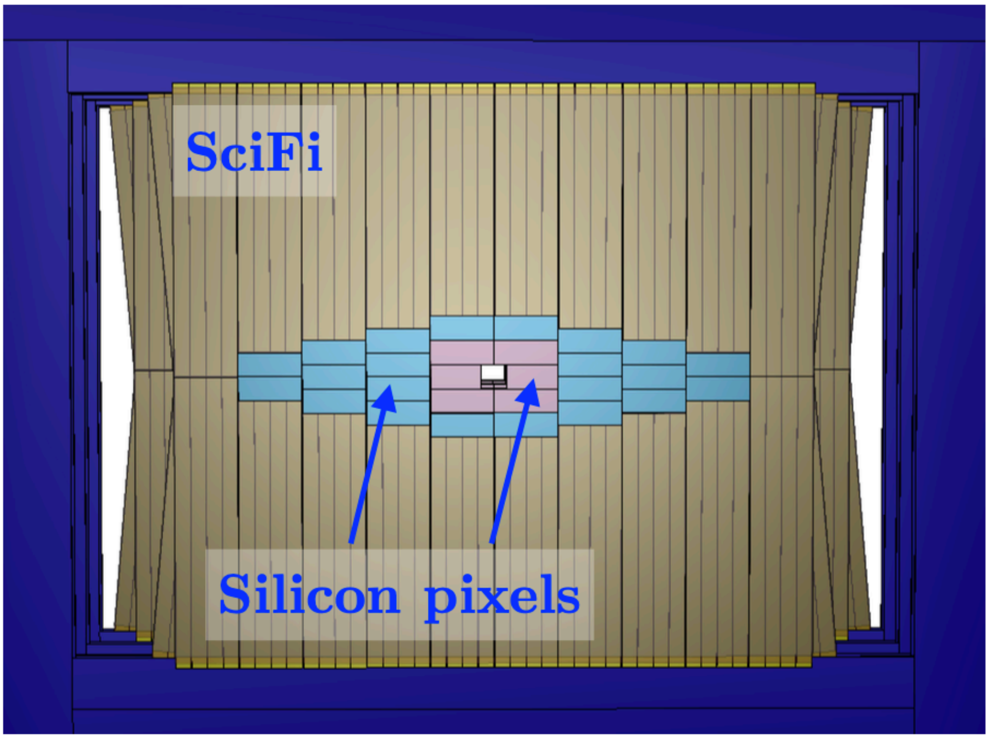

Figure 2.9: Schematic overview outlining the design of the Mighty Tracker [23].

ing fibre tracker, with inner regions of silicon pixel detectors (Inner Tracker and Middle Tracker) [24]. The proposed design of the Mighty Tracker is shown in Fig. 2.9.

2.2.1 MightyPix

The Mighty Tracker has proposed the use of MightyPix, which is a HV-MAPS sensor based on the MuPix8 and AtlasPix3 family of chips. The MuPix8 is used by the Mu3e experiment for the search of lepton flavour violation, and the AtlasPix3 is used by the ATLAS experiment. The MightyPix chip has dimensions of 20 mm x 20 mm and the size of each individual chip is determined by the reticle as part of the industrial manufacturing process. The chip features pixels measuring 50 µm x 150 µm, with increased granularity for the pixels in the bending plane of the LHCb magnet [25].

The HV-MAPS chips, such as the MightyPix are designed to withstand high levels of radiation exposure without significant degradation in performance, ideal for the environment in which the inner regions of the Mighty Tracker will operate. These chips also provide high spatial resolution, allowing for precise and accurate detection of particle tracks. The chips have the readout electronics directly integrated on to the same chip as the pixel sensor. This reduces the complexity of the detector system and allows for a compact and lightweight design, this also helps in reducing the noise and signal degradation that can occur in long readout paths. HV-MAPS offer the potential for high fill factors, maximising the sensitive area of the pixel and enhancing detection efficiency. While specific fill factors can vary based on design parameters, an estimated 5% inactive area per layer due to inactive columns could be considered a reasonable baseline. [26].

In comparison to other technologies, HV-MAPS sensors have a restricted depletion depth of around 30 μm for silicon and a resistivity of 200 Ωcm at the baseline pixel size. As a result, geometric charge sharing caused by non-perpendicular impacts is minimised at the downstream tracking station for the projected track angles. In simulation experiments, the average cluster size was found to be extremely close to one pixel, with about 98% of tracks indicating a cluster size of one pixel . The chips typically have a lower power consumption as compared to other pixel sensors with the same dimensions [27].

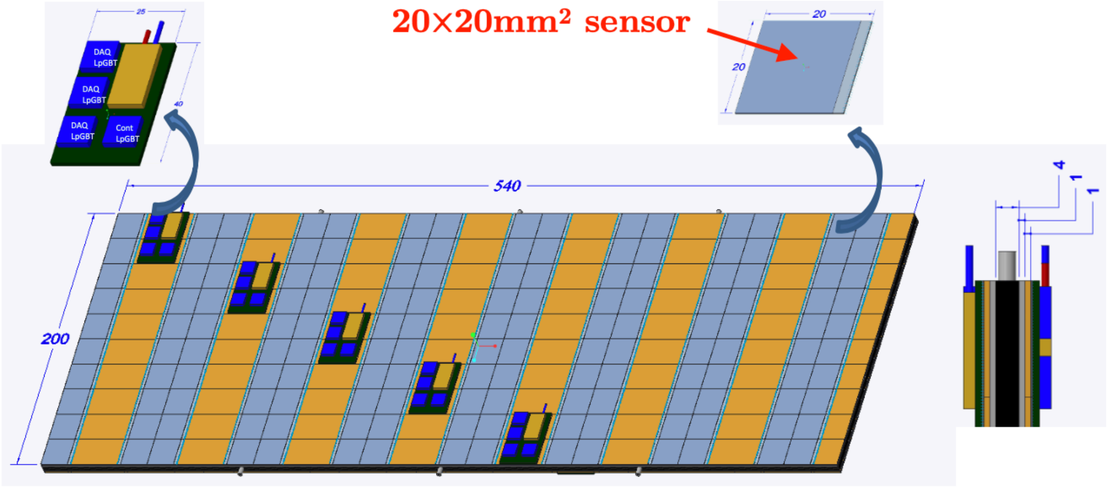

Figure 2.10: CAD model outlining the chip distribution on the Mighty Tracker module [23].

MightyPix pixels can be read individually but grouped in sets of four for bandwidth efficiency. Data is stored in binary zero-suppressed format using the 8b10b protocol for DC balance. The reference clock aligns with the control lpGBT, typically using 26-28 bits per hit, potentially fewer for baseline pixel dimensions [23]. MightyPix provides four output links at 1280 Mb/s each, with user-configurable options of one, two, or four links. Adjusting the reference clock allows for lower link speeds (640 Mb/s or 320 Mb/s), enhancing parallel processing in the subsequent readout stage [23]. The chip distribution on the Mighty Tracker module is illustrated using a CAD model in Fig. 2.10.

2.2.2 Mechanics

The Mighty Tracker modules consist of a carbon sandwich, with thin carbon fibre sheets (150 microns) co-cured with a thicker carbon foam slab (2mm) forming one module half. These halves are joined using carbon veil sheets and glue, housing the cooling pipe in the centre. The carbon foam slab provides mechanical support and structure to the carbon foam, it also has good thermal stability and is light weight. The carbon fibre and foam composites offer exceptional radiation resistance, ensuring prolonged structural integrity and detector functionality. Carbon fibre, in addition to foam, exhibits remarkable thermal stability, withstanding thermal cycling while preserving their form and characteristics across varying temperature conditions. Fig. 2.11 shows the cross-section of the Mighty Tracker module.

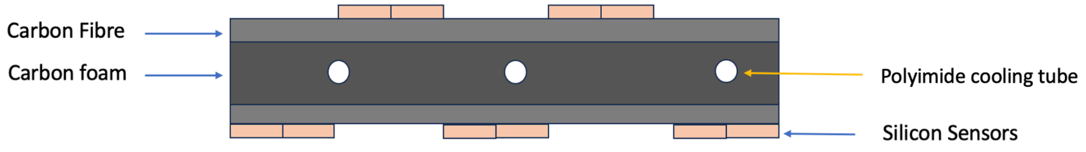

Figure 2.11: Schematic cross-section of the Mighty Tracker MAPS module.

The decision to incorporate carbon fibre in the detector's design was driven by the need for a material with several key attributes, including robust thermal conductivity, electrical insulation properties, precision manufacturability, low weight, and outstanding radiation resistance, all of which are satisfied by carbon fibre. In addition to their other properties, carbon fibre and foam possess short radiation lengths. This characteristic aids in minimising energy loss as particles traverse the detector, enhancing the likelihood of accurately detecting and measuring their properties. The Mighty Tracker places a high priority on minimising the material radiation lengths within its acceptance area, especially considering its impact on tracking efficiency due to particle scattering and secondary particles from the material. Table 2.1 shows the varying material radiation lengths for components within the Mighty Tracker modules.

Material	**Thickness (µm)**	$X_o\,(cm)$	X/X_o **(%)**	**Composite**
Carbon Fibre	150	23.7	0.08	C, K13C2U/EX-1515
Carbon Foam	4000	185.7	0.12	C, Allcomp K9 130pp
Cooling Pipes	76	28.6	0.01	Kapton Polyimide
Glue	100	35.5	0.03	TenCate EX-1515
Silicon	100	9.4	0.11	Si
SUM			**0.35**	

Table 2.1: Material radiation lengths for the components of the Mighty Tracker modules [18].

The Mighty Tracker is designed to utilise monophase cooling technology to maintain the detectors at a temperature below 0°C and the power requirements for the silicon sensors is 0.3 W/cm^2 (with a safety factor of two). At the outset, NOVEC coolants were proposed as the preferred coolant for the Mighty Tracker due to their outstanding dielectric properties, low viscosity, high heat capacity, chemical stability, and low boiling point [38]. However, the final decision on the type of coolant to be used has not been made, as the NOVEC coolants may be forbidden by new EU restrictions for Upgrade 2 and ongoing research and development are being conducted in this regard. In each module, there are connectors that link cooling pipes to those of adjacent modules within a support box. This arrangement allows multiple pipes inside the box to be combined into a single system. Essentially, all the cooling pipes in a support box are connected so that there is just one inflow pipe at the top of the box and one outflow pipe at the bottom. This design minimises the number of pipes passing through the detector's acceptance region. By doing so, it decreases the need to cover these pipes with insulation foam, such as Armaflex, which helps minimise the amount of additional material within the detector.

The mechanics for the Mighty Tracker, such as the metrology, cooling studies and X-Ray tomography studies are discussed in detail in Chapters 3, 4 and 5 respectively.

{Blank Page}

Chapter 3

Metrology

At LHCb, measurement accuracy is of paramount importance because precise measurements are not only instrumental in discovering new physics but also in rigorously testing the predictions of the Standard Model, searching for new particles, investigating rare processes, and deepening our understanding of fundamental particles and their interactions. Metrology, the science of precise measurement, is a fundamental pillar of our research. It plays a critical role in quantifying parameters essential for constructing and validating particle detectors and experimental setups. This section provides a detailed examination of the principles and applications of metrology within the framework of the Mighty Tracker's prototype modules.

3.1 Metrology Methodology

A SmartScope is a sophisticated and advanced measurement system engineered to conduct precise and automated inspections of diverse components and objects. By harnessing optical and imaging technologies alongside sophisticated software, it efficiently captures, analyses, and documents dimensional characteristics of the object being measured. In the context of conducting metrology on the Mighty Tracker prototype modules, this technology assumes a paramount role in meticulously assessing the module's dimensional attributes. At the University of Manchester, metrology is conducted using the OGP SmartScope Flash 300, which offers a precision of 5 µm in the z-axis and 2 µm in the xy plane. This accuracy is influenced by factors such as the relative height of the object being measured, the angle of the SmartScope's view, and the calibration of the system [28].

Equipped with advanced 3D scanning capabilities, the OPG SmartScope has the ability to create precise digital models for subsequent analysis of the measured samples. The machine uses non-contact measurement techniques like optical (camera) and laser scanning, to mitigate the risk of damage to sensitive components. Integrating into manufacturing processes, the SmartScope can facilitate real-time quality control and enable swift identification and correction of production-related issues. The SmartScope has various features that aid in the process of conducting metrology. The machine excels in precisely measuring dimensions, including length, width, height, diameters, and angles. Additionally, it offers geometric tolerancing capabilities to assess compliance with specific geometric tolerances, ensuring alignment with design specifications. The SmartScope can also be programmed to measure surface finish attributes, such as planarity and roughness. Fig. 3.1 shows the OPG SmartScope Flash 300, machine used for metrology at the University of Manchester.

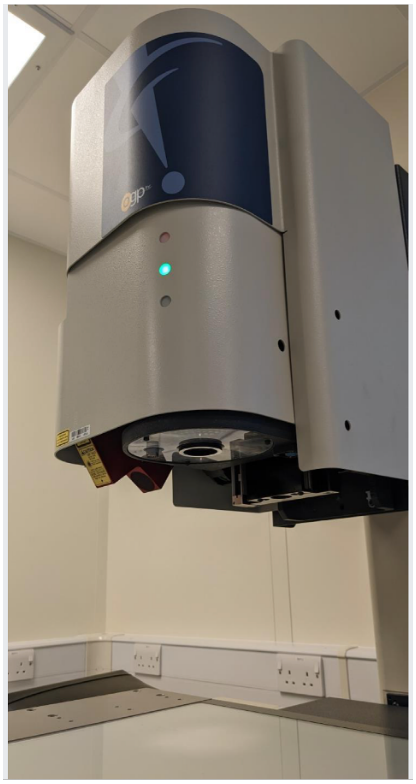

Figure 3.1: The OPG Smart-
Scope Flash 300 [27].

Both the SmartScope camera and laser are used to measure the thickness and planarity of the samples. The SmartScope has a flat measuring table with a backlight, that can move in the x and y direction. The head of the SmartScope (the top half that encompasses the camera and laser) moves in the z direction, and consists of different lighting features, which help the camera focus.

The metrology procedure involves preparing the samples for measurement, executing an automatic routine, documenting all measured values, and conducting subsequent analysis. The SmartScope operates using a predefined routine, essentially a program containing user-programmed instructions for the SmartScope's automated actions. This routine initiates by aligning the SmartScope camera's crosshair with the sample's edges, establishing the sample's position on the table. The SmartScope then aligns its crosshair with the top and bottom edges of the sample. Subsequently, a rough alignment is performed in the x and y directions, followed by another rough alignment in the x, y, and z directions . The SmartScope proceeds to measure the sample's perimeter by fitting a line to the dataset captured by the camera along the edges of the sample. This process establishes two fixed intersection points, one at the bottom left and the other at the top left as shown in Fig. 3.2, which serve as reference points. Using these reference points, the SmartScope executes a precise alignment in the x, y, and z directions. Subsequently, the routine is configured to measure reference lines around the sample using the SmartScope laser. The laser plots multiple points, spaced 100 microns apart in a line. This process is repeated for all reference lines. The SmartScope then uses these lines collectively to form a reference plane, and a final alignment is conducted. Following this alignment, the SmartScope's laser or camera measures the sample from bottom to top, collecting data points in a grid pattern. Once the measurements are completed, the data from the reference and sample lines are recorded in a .txt file for analysis.

During all SmartScope measurements, the sample is positioned on top of two rubber O-rings. These O-rings serve a dual purpose: they ensure the sample's stability, preventing any slippage on the smooth glass surface of the SmartScope, while also elevating the sample to an optimal height for laser focusing. Additionally, a silicon wafer is positioned on top of the O-rings, serving as a smooth and flat reference plane. This configuration enables precise measurement of the sample's thickness and planarity. The sample set-up for the SmartScope is shown in Fig. 3.2.

The metrology process for the Mighty Tracker prototype modules involves assessing the thickness and planarity of the co-cured carbon foam and carbon fibre halves. This

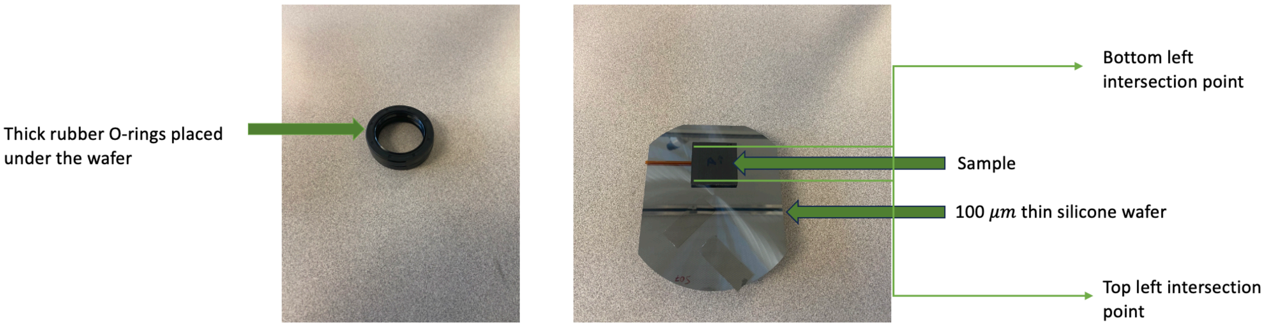

Figure 3.2: SmartScope sample set up.

assessment ensures that during the assembly phase, where the two halves are bonded together to create an unified structure, the samples remain free from any bending or bowing in any plane. Furthermore, it measures the flatness of the channel for the cooling pipe, ensuring it maintains a deviation of less than 2 degrees from a perfectly flat plane (silicone wafer) and a consistent channel width across the samples. Following the assembly process, measurements of sample thickness and planarity are taken. These measurements serve the purpose of evaluating the quantity of glue used. By zooming in at the edges of the sample with the SmartScope camera, any excess glue that may have overflowed from the sides of the samples can be identified. Additionally, these measurements help in detecting any potential warping or bowing of the samples once the glue has cured. The complete details of the metrology process for the samples, both before and after assembly, are thoroughly discussed in sections 3.2 and 3.4, respectively.

3.1.1 Thickness and Planarity Measurement

The SmartScope employs a laser to measure the reference plane on the silicon. This plane is determined by creating three lines positioned 2mm from the sample, extending from the bottom, top, left, and right sides, mirroring the sample's length, as shown in Fig. 3.3. These reference lines are utilised to construct a plane on the thin silicon wafer. A secondary set of lines/points is recorded on top of the sample. Depending on the focus of each sensor, these lines/points can be captured by the camera and/or the laser. They originate at the bottom of the sample and extend to the top, with the sensors acquiring points from left to right across the sample. These lines/points are then used to establish a plane that corresponds to the sample plane. The thickness is subsequently determined as the mean of all distances between the reference plane and the sample plane. The thickness measurement's error is determined by the standard deviation of these distances. Fig. 3.3 gives a description of how thickness is measured and calculated.

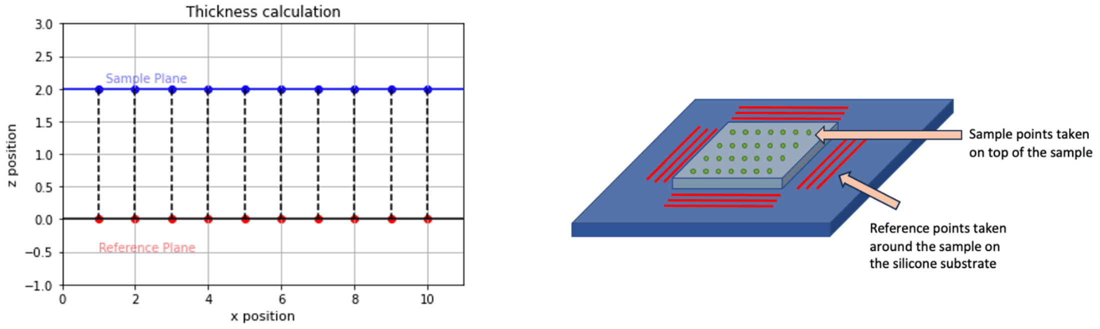

Figure 3.3: **Left panel:** A 2D representation of the thickness calculation. The blue line represents the sample plane, while the red line represents the reference plane. The vertical axis (z) represents the height, and the horizontal axis (x) represents the position. The blue dots indicate sample points taken on top of the sample, and the red dots represent reference points taken around the sample on the silicone substrate. Dashed lines indicate the calculated thickness between corresponding sample and reference points.
Right panel: A 3D schematic of the measurement setup. The blue rectangular object represents the silicone substrate, and the red rectangular object on top represents the sample. The red dots and lines indicate the positions where sample points are taken, and the orange arrows show the direction of measurement.

The measurement of planarity involves several steps. Initially, a best-fit plane is determined by analysing the sample points taken from the top of the sample. Subsequently, for each individual point, a positive or negative deviation from this best-fit plane is calculated, with the plane itself serving as the reference plane (set at zero deviation). This process results in a planarity measurement for each point on the sample.

To evaluate the planarity for the entire sample, the standard deviation of these individual point deviations from the best-fit plane is calculated. This standard deviation provides an overall measure of how flat or planar the sample is, considering the deviations of all the sample points from the sample plane.

The SmartScope camera measures the thickness on the carbon foam side by taking multiple grid-like measurements across the foam, excluding the channel for the cooling tube. Subsequently, a grid of reference lines is captured by the laser on the silicon wafer to establish the reference plane, as depicted in the diagram in Fig. 3.3. additionally, the camera is used to measure the width and angle of the channel for the cooling tube. For the foam side the SmartScope camera is preferred over the laser because the laser struggles to focus on and gauge the depth of the foam due to its uneven and rough surface. For the carbon fibre side, since it has a smooth surface, both the laser and the camera can be used for measuring the thickness and planarity. The laser is employed to measure a corresponding grid of reference lines on the silicon wafer, followed by the measurement of a grid of lines across the carbon fibre surface.

The thickness of the co-cured samples was measured using both the SmartScope camera and laser. The camera captured a grid of points across the sample, while the laser scanned a series of lines with a 100-micron spacing. This difference in measurement resolution resulted in a systematic discrepancy of approximately 100 microns between the two methods. While the laser data provides a more precise measurement of the sample thickness, the camera data offers complementary information about the sample's overall geometry.

3.1.2 Smart-Scope Calibration

To ensure the reliability of the measurements obtained with the SmartScope, a calibration measurement of thickness and planarity was performed on a Grade 1 steel block, which had a thickness tolerance of 10 microns and was 4mm thick, as shown in Fig. 3.4. The block was measured using the same setup employed for measuring the Mighty Tracker samples. A routine similar to the one utilised for measuring the samples was developed to measure the thickness and planarity of the block. After executing the routine, the thickness of the block was determined to be (4.010 ± 0.002) mm, a measurement that falls within the specified tolerance (±0.010) mm provided by the manufacturer. Additionally, the planarity of the block was measured to be ±0.001 mm. To confirm the repeatability of the process, the calibration was performed twice on the same steel block, yielding consistent results. The block was removed and replaced on the silicon wafer between each measurement to assess the impact of repositioning on measurement consistency. The SmartScope was maintained in a stable environmental condition throughout the calibration process. This process serves the crucial purpose of verifying the correct functioning of the entire measurement system, including the setup, the programmed routine, and the subsequent data analysis. Moreover, it ensures that the system consistently produces reliable and repeatable results, thereby enhancing the credibility of the measurements obtained.

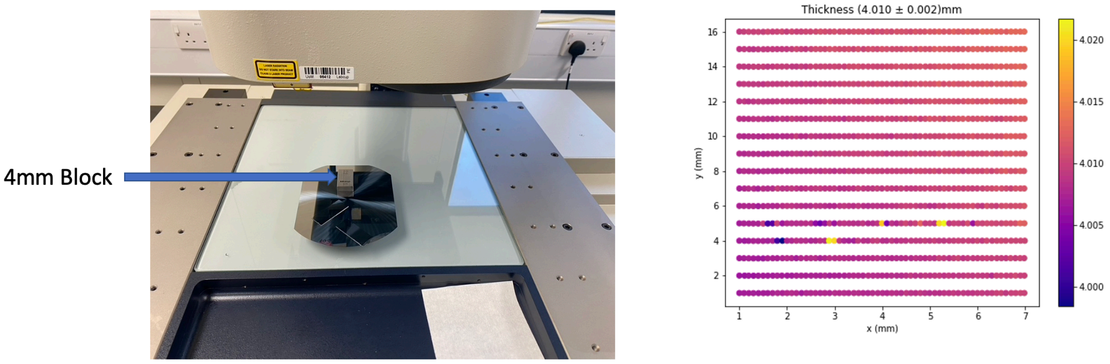

Figure 3.4: Left: Experimental setup for measuring the thickness of a 4 mm steel block using the SmartScope. Right: Scatter plot of thickness measurements across the block, demonstrating a mean thickness of 4.010 mm with a standard deviation of 0.002 mm. The colour scale represents thickness variation.

3.2 Co-Cured Samples

The co-cured prototypes for the Mighty Tracker pixel modules consist of two materials: carbon foam and carbon fibre sheet. The carbon foam measures 2 mm in thickness and has dimensions of 40 mm x 40 mm. This material is sourced from Lockheed Martin. The carbon fibre sheet is 150 µm thick and shares the same dimensions of 40 mm x 40 mm.

The carbon fibre sheet is constructed using three layers of carbon fibre arranged in a 0-90-0 orientation. The carbon fibre sheets are impregnated with resin during their manufacturing process. These resin-filled carbon fibre sheets are then placed onto the carbon foam. Subsequently, the carbon sample is placed within a vacuum and subjected to heat to facilitate the curing process. Following the curing process, the sample is machined on the foam side to create a groove in the middle. This groove is designed to accommodate the polyimide cooling tube when the sample is glued together. Fig. 3.5 shows the co-cured samples.

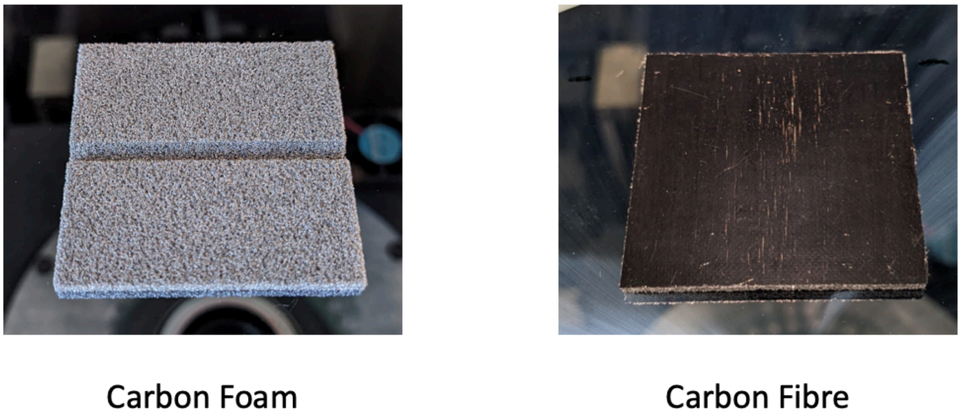
Carbon Foam

Carbon Fibre

Figure 3.5: Images showing the Co-Cured samples of carbon foam and carbon fibre.

Once the samples have fully cured, metrology was performed on both halves using the SmartScope, following the procedure outlined in Section 3.1.1. The thickness of the carbon foam side was determined by analysing the camera data, while the laser was used to establish a reference plane and measure the carbon fibre side due to its smoother surface.

After completing the measurements, the data obtained from the reference lines and sample lines are analysed using a Python script. This script employs the method detailed in section 3.1.1 to determine the thickness and planarity of the samples. The results are presented through a scatter plot for thickness and a 1D histogram for planarity. These visualisations are displayed for both the foam and fibre samples in Fig. 3.6 and Fig. 3.7 respectively. In Fig. 3.7 (right), A significant deviation of three standard

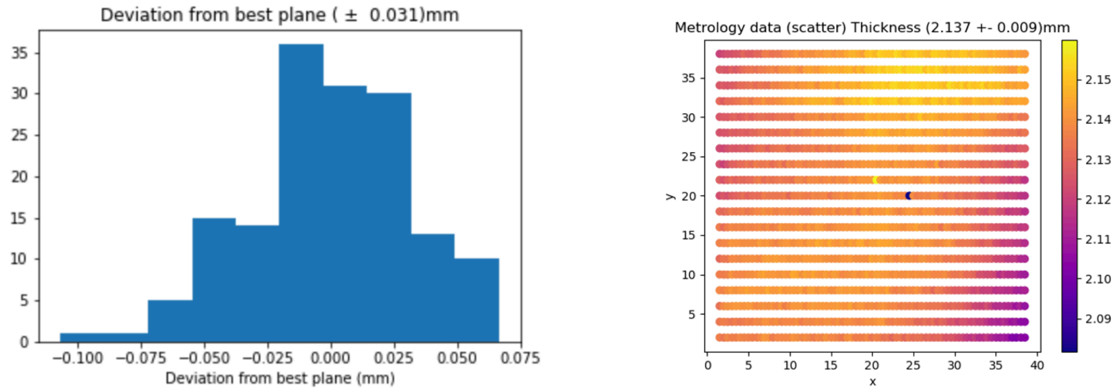

Figure 3.6: **Left:** Histogram of deviation from the best-fit plane for all measured points. The distribution exhibits a mean deviation of ±0.031 mm.

Right: Scatter plot of measured thickness across the sample. The colour scale represents thickness variation, with a mean thickness of 2.137 mm and a standard deviation of 0.009 mm.

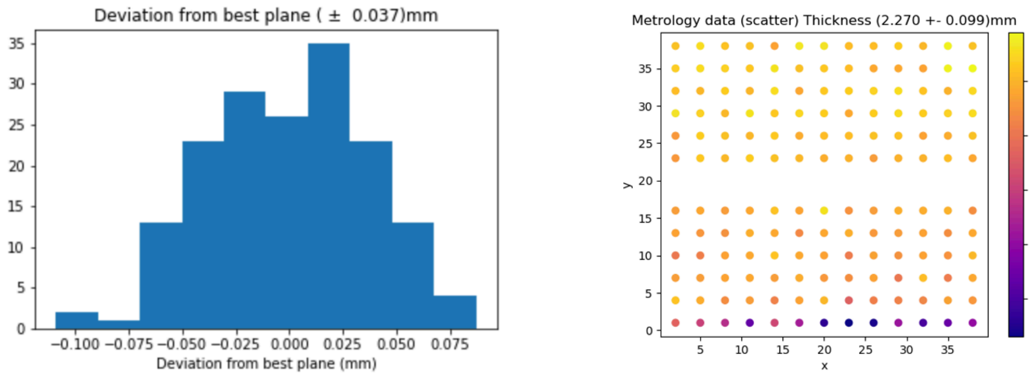

Figure 3.7: **Left:** Histogram of deviation from the best-fit plane for all measured points. The distribution exhibits a mean deviation of ±0.037 mm.

Right: Scatter plot of measured thickness across the sample. The colour scale represents thickness variation, with a mean thickness of 2.270 mm and a standard deviation of 0.099 mm.

deviations from the mean thickness is evident at the beginning of the sample, specifically for sample number 12. This deviation is a result of a non-uniform underlap of carbon fibre on the foam side. The unevenness in the carbon fibre underlap is attributed to irregular cutting of the carbon foam. When the foam was co-cured with the fibre, the region with rough edges on the foam did not completely cover the carbon fibre layer, leading to an anomaly in the thickness measurement, where the foam thickness is smaller than in other regions. There are eight co-cured samples and this process was repeated for all eight co-cured samples, involving measurements on both the carbon foam and fibre sides. While the inclusion of the anomalous data point from Figure 3.7 might skew the overall average, it is essential for understanding the full range of thickness variations within the sample set. The average thickness measured on the foam side was found to be 2.261 mm, while on the fibre side, it was 2.162 mm. Additionally, the average planarity was calculated to be ±0.037 mm for the foam side and ±0.031 mm for the fibre side. The planarity measured for the foam is slightly higher than that for the fibre due to the presence of a large number of small bubbles in the foam, resulting in a greater planarity value. Analysis of the planarity data revealed no significant deviations from flatness exceeding 100 microns across the sample surface, it was determined that there were no significant indentations or bowing observed in the samples, whether from the foam or the fibre side. Eight samples were paired and co-cured to create four carbon sandwiches. To ensure consistency, the thickness of each sandwich was targeted to be within a 100-micron range. The predicted average sandwich thickness was 4.326 mm, with a tolerance of ±0.040 mm. However, given the inherent variability in the manufacturing process, actual thicknesses varied slightly between sandwiches.

3.3 Module Assembly and Curing Process

Following metrology, which revealed minor irregularities in sample planarity as depicted in Figure 3.7, the assembly process commenced. While these imperfections did not significantly impact the overall module flatness (<100 microns), they were considered during the assembly process to minimise their potential influence on module performance. The module assembly process utilises a combination of co-cured samples, carbon veils, and a polyimide cooling tube as primary components. Essential tools and materials include an aluminium base plate, spreader plate, and a variety of small components such as metal spacers, a glueing brush, and a metal rod. Consumables like epoxy adhesive, catalyst, graphite powder, gloves, and cleaning agents (acetone and isopropanol) are also required for the assembly and preparation process. The carbon veils serve

as intermediaries for the adhesive to create an even bond between the two samples. They facilitate the uniform distribution of glue between the two halves, ensuring a strong connection. The adhesive of choice is Hysol Loctite EA 9396 AERO industrial epoxy glue, consisting of two parts: epoxy and a catalyst (hardener). Graphite powder is added to the glue mix to improve thermal conductivity around the cooling tube.
The assembly process starts with the meticulous cleaning of all components, including the brush, base plate, spreader plate, spacers, cooling tube, vacuum table, and work table, using acetone and isopropanol. Additionally, the co-cured samples are vacuumed to remove any loose carbon dust from their surfaces. Once all components are thoroughly cleaned, the bottom half of the sample is positioned on the base plate along with the cooling tube inserted in the channel, marking the sample’s positions as a reference point to ensure proper alignment during assembly. After alignment, the cooling tube is marked and trimmed to the required length (which is about three times the length of the sample). During the cutting process, an insulated copper wire is inserted into the tube to prevent bending at the cut end. The assembly process continues by mixing the two components of the glue. Specifically, 5g of epoxy is blended with 1.5g of the catalyst in a planetary mixer for a duration of 3 minutes at 2000 rpm. Once the glue is thoroughly mixed, it is evenly spread onto the carbon veils using a glue brush as shown in Fig. 3.8. These veils are then positioned on the bottom half of the sample. Subsequently, 30% of the glue's weight in graphite powder is added to the glue mixture and mixed in the planetary mixer for another 3 minutes, this time at 3000 rpm. Following this, 0.27g of glue is applied to the cooling tube using a swab. A metal rod is carefully inserted into the cooling tube to prevent it from bending during the curing process within the vacuum. The bottom half, with the carbon veils in place, is then positioned on the base plate and aligned using the reference marks. Subsequently, the glue-covered cooling tube is inserted into the channel of the bottom half, and the top half of the sample is placed on top and pressed down securely, as illustrated in Fig. 3.8.

The assembled unit is then transferred to the vacuum table. Spacers are strategically placed along the sample, as depicted in Fig. 3.8. Once the spacers are correctly positioned, the spreader plate is gently set atop the assembly. Final checks are conducted to ensure nothing has shifted and the spacers are not in contact with the sample. Subsequently, the vacuum membrane is lowered into place. This membrane, crafted from neoprene, which is a soft yet resilient fabric, is airtight and conforms to the shape of the spreader plate when vacuum pressure is applied. This ensures uniform pressure on top of the module during the curing process. The sample is allowed to cure under vacuum conditions for a period of 24 hours. Upon completion of the curing process, the two halves are labeled as side A and side B, and the sample is weighed (after accounting for potential glue mass loss due to evaporation) to determine the amount of glue utilised during the procedure. The process is repeated three more times to produce a total of four sandwiches/modules.

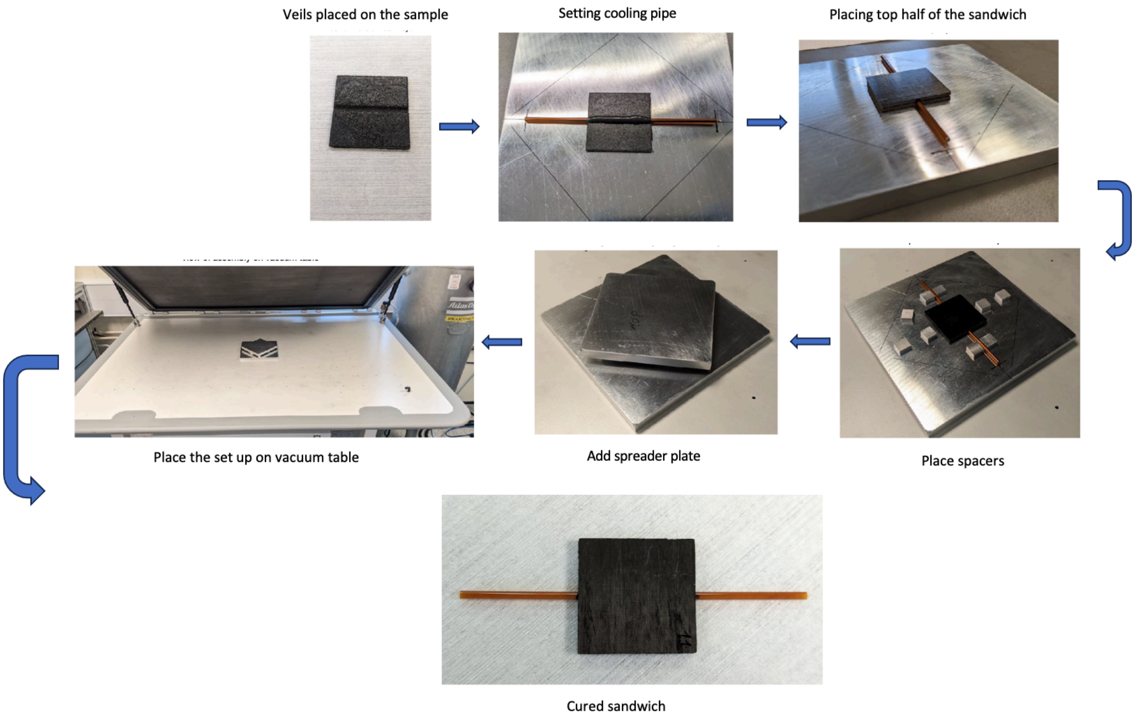

Figure 3.8: The figure outlines the sequential steps involved in assembling the prototype modules. The process begins with the placement of carbon veils on the bottom half of the sandwich, followed by the insertion of the cooling pipe. The top half of the sandwich is then added, and the entire assembly is placed on the vacuum table. The use of spacers and a spreader plate ensures uniform pressure distribution during the curing process under vacuum. The final image depicts the fully assembled and cured sandwich.

3.4 Sandwich Metrology

The metrology of the module prototype is similarly conducted using the SmartScope, employing the setup shown in Fig. 3.2. This metrology process encompasses both side A and side B of the sandwich and involves the use of the SmartScope laser. The procedure closely mirrors the one employed for the metrology of the carbon fibre side of the co-cured modules (discussed in section 3.2), with a minor adaptation involving the three reference lines on the right and left sides of the module.

Since the cooling tube traverses the sandwich, the laser encounters difficulty focusing when it encounters the tube. To address this challenge, the reference lines are divided into two segments. The first segment extends from the corner of the sandwich to 1mm before the tube, where the laser can effectively focus. The second segment covers the 1mm region after the pipe and extends to the top corner of the sandwich, as shown in Fig. 3.9. This modification ensures accurate metrology despite the presence of the cooling tube. The process is repeated for all the reference lines from the right and left sides. After the routine is adjusted, the metrology is conducted for the sandwiches in multiple runs for each side with variation in position on the SmartScope table. This was done to check the repeatability and consistency of the measurements, and if small changes in position effect the overall result of the thickness and planarity.

The routine is executed, and measurements for the reference lines and sample lines are recorded for one side. This process is then repeated twice without altering the position. After the third run, the sandwich's position on the SmartScope table is changed. A total of six runs are conducted on each side, with three runs maintaining the same position and three involving position changes. The process is repeated for two sandwiches. After analysing the measurements using python, it was found for sandwich one, after the first run with no change in position, the thickness dropped by 1 micron for both sides but remained consistent thereafter. Sandwich two exhibited a more pronounced thickness reduction of approximately 10-12 microns after the second measurement cycle, as illustrated in Fig. 3.10. While these variations exceed the desired tolerance of ±10 microns, a thorough analysis of potential error sources, including comparing measurement uncertainties and manufacturing tolerances, revealed that the error of ±10 microns can be attributed to measurement error. Given the overall sand wich thickness and the preliminary nature of this study, these variations are considered manageable at this stage, but warrant further investigation in subsequent iterations.

To investigate the potential impact of environmental factors like temperature and humidity on sample measurements, the metrology for two sandwiches was repeated with variations in temperature. Five measurement runs were conducted for each side of sandwich one and two, with ambient temperature fluctuating between $10^\circ C$ and $15^\circ C$ during the experiment. Analysis of the measurements revealed that while temperature fluctuated during the runs, these variations did not consistently correspond to changes in thickness. Data from Figure 3.10 (Side B at $13.5^\circ C$) reveals thickness measurement variations of approximately ±10 microns, even under controlled temperature conditions. This suggests that temperature fluctuations had a minimal impact on the overall sample thickness.

With no effects from environmental factors and change in position, the metrology was conducted for four sandwiches on each side. The recorded data was analysed and the mean thickness and planarity were calculated for each side for each sandwich. The average thickness of four sandwiches was found to be (4.322 ± 0.008) mm, with a consistent average planarity of 5 microns. The scatter plot for the thickness and planarity is shown in Fig.3.11. Planarity remained stable throughout the metrology of all sandwiches, with only a 2-micron variation between samples. This indicates that there was no noticeable bowing in the sandwiches after the vacuum curing process, and the glue application did not introduce any significant irregularities, which suggests that the assembly and the metrology method is reliable and repeatable.

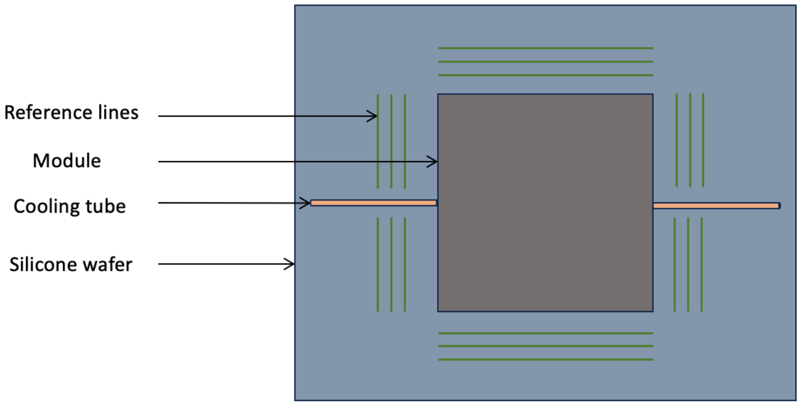

Figure 3.9: The above diagram illustrates the experimental setup for measuring the thickness of the sandwich modules. The modules are placed on top of a silicone wafer. To avoid interference with the thickness measurement, the reference lines bypass the pipe area. This configuration allows for precise thickness determination based on the distance between the reference lines and the module surface.

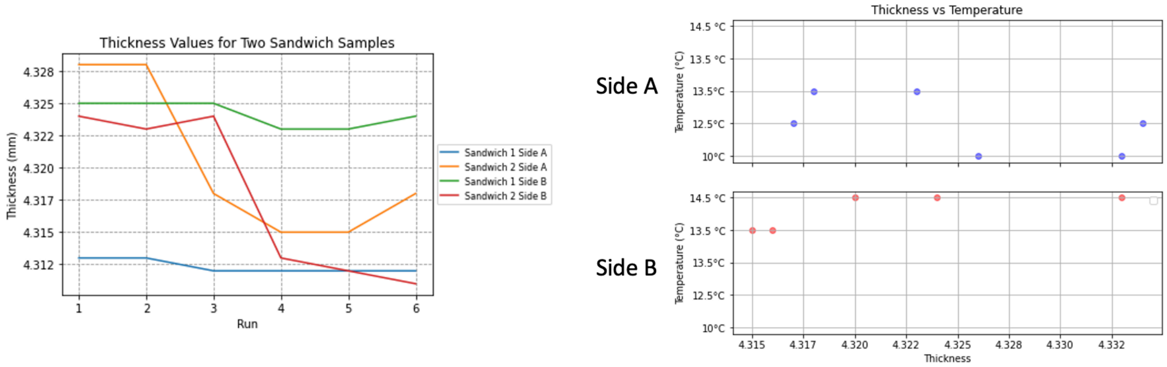

Figure 3.10: The figure illustrates the thickness variation for two sandwich samples across multiple runs at different temperatures. The left panel shows the thickness evolution with run number, while the right panel demonstrates the thickness dependency on temperature.

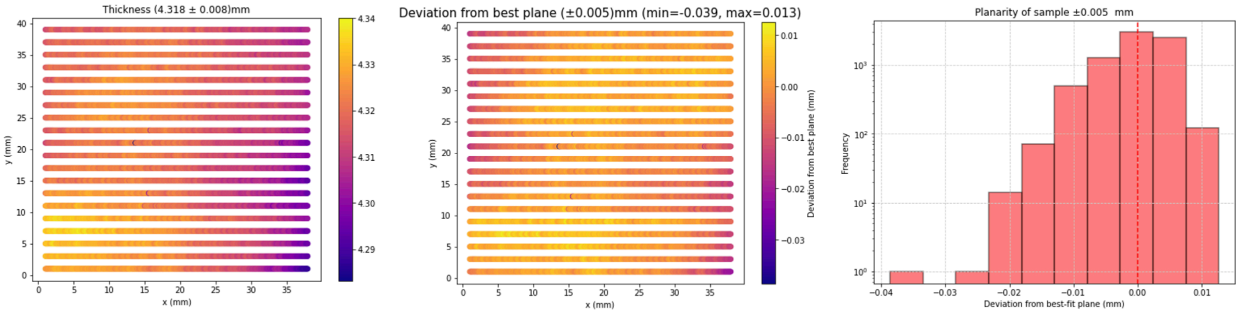

Figure 3.11: This figure presents a visual representation of thickness and planarity for Sandwich 2. The left panel displays a colour-coded thickness map, revealing variations across the sample. The middle panel shows the deviation from the best-fit plane, highlighting areas of non-planarity. The right panel provides a histogram of planarity deviations, summarising the overall flatness of the sample

3.5 Summary

This chapter focuses on the metrology procedures employed to characterise the Mighty Tracker prototype modules. The chapter begins by introducing the SmartScope, a critical instrument used for precise measurements. The metrology methodology, including sample preparation, measurement process, and data analysis, is detailed.

Key findings include:

- Successful measurement of sample thickness and planarity using the SmartScope.
- Identification of potential thickness variations due to manufacturing inconsistencies.
- Assessment of environmental factors (temperature) and their minimal impact on measurements.
- Consistent planarity across all samples, indicating successful assembly and curing.
- Establishment of a reliable metrology process with repeatable results.

Potential areas for further investigation include refining the metrology process to reduce measurement uncertainties, exploring the impact of different glue types or curing conditions on sample properties, and Optimising the assembly process for increased efficiency

{Blank Page}

Chapter 4

Thermal Studies

The operation of the Mighty Tracker detector at LHCb requires meticulous thermal management to prevent sensor overheating and ensure long-term efficiency. To meet this requirement, simplified thermal calculations (calculating temperature difference and heat transfer) are employed to establish baseline temperature (temperature values used as reference for cooling tests) values for the current prototype module. These calculations serve as a diagnostic tool to identify any necessary modifications to the module's mechanics. Complementing the thermal simulations, finite element analysis (FEA) is conducted to validate the simulation results. Once an agreement is achieved between the thermal calculations and FEA values, cooling studies are performed on prototype modules to assess their behaviour under elevated temperature conditions and test the validity of the results found theoretically. The thermal calculations serve multiple purposes, addressing critical aspects of Mighty Tracker's thermal management. They determine the number of necessary cooling pipes to maintain sensors at temperatures around 0°C as this is the ideal temperature for optimal sensor operation, optimise the cooling capacity for each pipe, select an appropriate coolant to avoid over or under-cooling, and identify potential design enhancements to improve thermal stability and meet operational requirements.

4.1 Simplified Thermal Model

In the thermal studies, a simplified model of the current Mighty Tracker prototype is employed, guided by several strategic assumptions aimed at simplifying calculations. To simplify the thermal model, the symmetrical nature of the prototype module allowed for the analysis of a single quadrant, assuming identical properties across all four sections. While edge effects could potentially influence the temperature distribution, this simplification provides a reasonable approximation for initial analysis. The power coming from the chip is assumed to be constant. The model follows a simplified geometry, neglecting contributions from the foam and fibre over the pipe as shown in Fig. 4.1.

This simplification is justified by the very small thickness of the foam and fibre over the pipe, which has negligible effects on the overall temperature difference. Additionally, since the foam has isotropic thermal conductivity, the model presumes bi-directional heat flow, with one direction of heat flow moving vertically from the chip into the foam and the other proceeding longitudinally or horizontally across the foam toward the pipe, as can be seen in Fig. 4.1. These assumptions collectively streamline thermal analyses and simplify calculations.

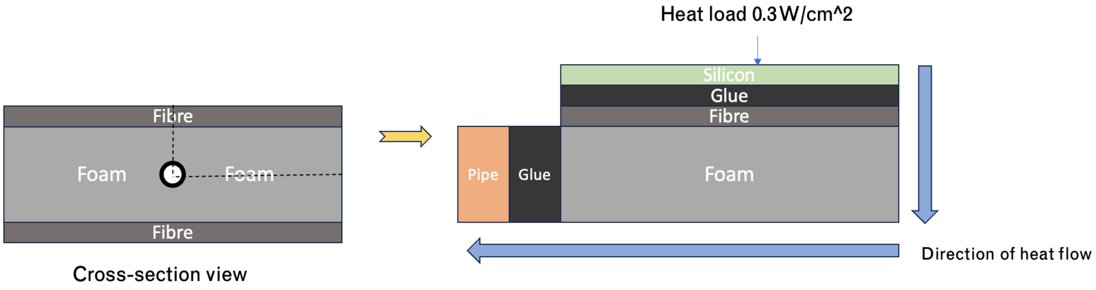

Figure 4.1: Cross-sectional schematic of the simplified thermal model for a single chip. The figure illustrates the heat flow path through the different material layers of the prototype module. A constant heat load of 0.3 W/cm² is applied to the silicon chip. Heat is conducted through the glue, fibre, and foam layers before being dissipated by the cooling pipe. The simplified model assumes symmetrical heat distribution and neglects heat losses through the top and bottom surfaces of the module.

The model serves to compute the temperature difference, a factor of ΔT, for each component. In the case of vertical heat flow, heat traverses through the thickness of the components, including silicon, glue, fibre, and foam. Conversely, in the scenario of longitudinal heat flow, heat propagates along the length of the components, which encompass foam, glue, and the pipe. Notably, this model assumes that the foam makes two distinct contributions to the overall ΔT of the module. The model dimensions are approximately 100 mm x 20 mm x 4.4 mm, and the modelling is entirely done in Python.

The calculations for ΔT are all done using the Fourier's Law of heat transfer [29], which states that the rate of heat transfer through a solid material is directly proportional to the temperature difference across the material and is inversely proportional to the distance over which the heat travels. The equation is given by,

$$P = k \times A \times \frac{\Delta T}{L} \rightarrow \Delta T = \frac{P \times L}{k \times A} \tag{6}$$

Where P is the power produced by one chip in watts (W), k is the coefficient of thermal conductivity of the material, measured in $\mathrm{Wm^{-1}K^{-1}}$, it represents the material's ability to conduct heat, A is the cross-sectional area through which the heat is transferred, measured in m^2 and L is the thickness or the length across which the heat is conducted, measured in m. The ΔT is measured in units of Kelvin. The relation shows that the temperature difference (ΔT) is directly proportional to the distance (L) over which the heat travels, which implies, larger the value of L, larger is the value of the temperature difference. The power density of one chip is 0.3 W/cm^2 (with a safety factor of 2), which equates to a power output of 1.2 W for the area of one chip with dimensions of 20 mm x 20 mm.

4.1.1 Vertical Flow of Heat

The temperature difference for the components through which heat flows vertically is determined using equation (6). Key parameters, including dimensions and coefficients of thermal conductivity, along with the value of ΔT, are detailed in Table 4.1. Thermal conductivity values for the various components were obtained from [30].

Components	Length (m)	Width (m)	Thickness (m)	Thermal Conductivity ($\mathrm{Wm^{-1}K^{-1}}$)	ΔT (K)
Silicon	0.02	0.02	1.0×10^{-4}	148	0.0002
Glue	0.02	0.02	1.0×10^{-4}	1.0	0.300
Fibre	0.02	0.02	1.5×10^{-4}	1.2	0.375
Foam	0.02	0.02	4.0×10^{-3}	40	0.300

Table 4.1: Key Parameters and Calculated ΔT Values (Vertical Heat Flow, power of 1.2 W).

The direction of heat flow is through the thickness of the components, meaning that in equation (6), L represents the thickness of the material. Furthermore, the cross-sectional area is computed as the product of the length and width, a result of the model's geometry. Table 4.1 shows that the contributions of ΔT from all the components with vertical flow are minimal, and they do not significantly impact the overall ΔT of the model. Given the significantly smaller thickness of the fibre and glue layers compared to the characteristic length for heat conduction, the resulting temperature rise (ΔT) within these elements is negligible compared to the temperature rise of the bulk components experiencing horizontal heat flow.

4.1.2 Lateral Heat Transfer

The temperature difference for the components through which heat flows horizontally (foam, glue, and pipe as shown in Fig. 4.1) is computed using the same approach as before, applying equation (6). The key difference lies in the fact that heat now propagates along the length of the module with the same power of 0.3 W/cm^2, making the ΔT a function of length rather than thickness. The parameters used for the calculation are shown in Table 4.2.

Components	Length (m)	Width (m)	Thickness (m)	Thermal Conductivity (Wm^{-1}K^{-1})	ΔT (K)
Foam	0.1	0.02	4.0×10^{-3}	40	37.50
Glue	0.004	0.02	1.0×10^{-4}	1.0	1.500
Pipe	0.009 (circumference)	0.02	7.6×10^{-5}	1.3	0.372

Table 4.2: Key Parameters and Calculated ΔT Values (Horizontal Heat Flow, power of 1.2 W).

In the context of horizontal heat flow, it is evident that the ΔT for the foam component exerts the most dominant influence on the overall ΔT of the model. Due to the linear relationship between L and ΔT, the impact of thermal conductivity on heat transfer is significantly greater than that of other material properties. Conversely, for the glue layer, the reduced area, coupled with the inverse relationship between ΔT and area, results in a larger temperature difference compared to when heat flowed vertically. Nevertheless, the contribution of the glue layer, while larger, remains less significant in affecting the overall ΔT of the model in comparison to the foam component. The ΔT of the pipe is insignificant, similar to the calculations done for the fibre and glue components in the previous section. The pipe's thin wall thickness minimally impacts the overall ΔT, especially over short distances. The model employs a lumped analysis approach, neglecting the temperature variation across the thin pipe wall. This approach assumes a uniform temperature throughout the wall due to its small thickness, especially for short distances. Consequently, the wall's contribution to the overall thermal resistance is considered negligible.

Based on the model calculations, it is evident that the foam component plays a dominant role in contributing to the overall ΔT for the model. The fibre component exhibits an exceptionally low coefficient of thermal conductivity when heat flows vertically. It is important to highlight that the module's fibre component is constructed by stacking sheets of carbon fibre in a 0-90-0 orientation. This orientation imparts different values of thermal conductivity to the material, depending on the direction of heat flow. Consequently, the model can be extended to assess both the foam and fibre contributions to ΔT when heat flows horizontally. This extension allows for a more comprehensive analysis of temperature differences within the module.

4.1.3 Impact of Fibre Orientation on Thermal Conductivity

The carbon fibre component exhibits two distinct thermal conductivities, contingent on the direction of heat flow. Through the plane, the thermal conductivity is 1.2 $\mathrm{Wm^{-1}K^{-1}}$. However, when heat flows horizontally (in plane), the thermal conductivity substantially increases to 1000 $\mathrm{Wm^{-1}K^{-1}}$. This significant difference in values arises from the layered structure of the carbon fibre slab, which is a result of the layered fabrication process. To consider the unique thermal properties of the fibre component, a separate model is simulated, resembling the basic model. In this model, the heat load from the chip is directed horizontally, and the fibre is stacked on top of the foam. The power is distributed between the fibre and foam, and these two components are in contact with distinct temperature reservoirs at each end, each maintained at temperatures, T_1 and T_2, and $\Delta T_1 = \Delta T_2$. The model schematic is shown in Fig. 4.2.

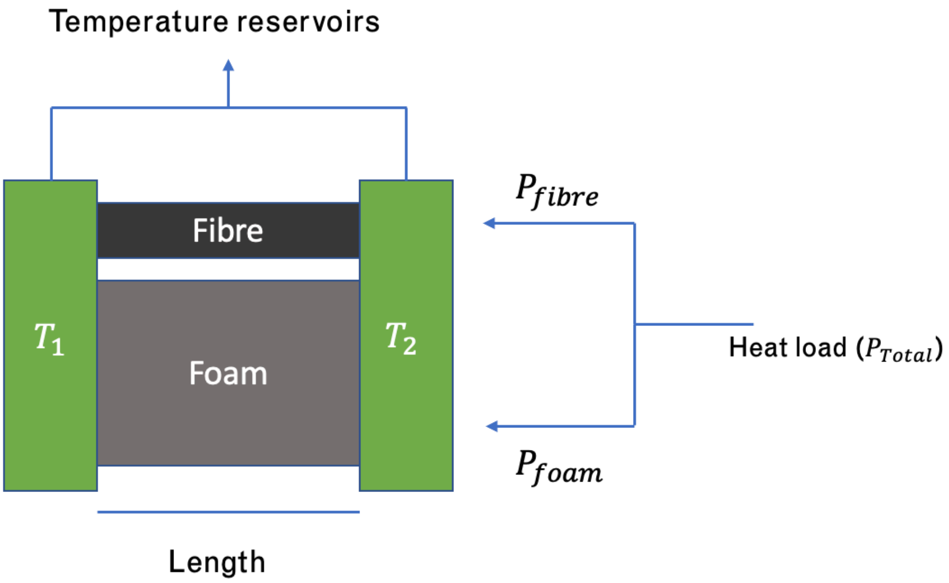

Figure 4.2: Schematic of the 1D thermal model for foam and fibre. The figure illustrates a simplified model of heat transfer through the foam and fibre layers. A constant heat load (P_{Total}) is applied, resulting in temperature gradients across the materials. The model assumes one-dimensional heat flow, with boundary conditions defined by temperature reservoirs (T_1 and T_2).

With heat flowing horizontally, the ΔT for both the fibre and foam components is computed using equation (6), under the heat load of one chip 1.2 W. The parameters remain consistent with those used previously, except for adjusting the length parameter for the fibre component to match that of the foam and modifying thermal conductivity to account for the directional dependence of the fibre's thermal properties. The parameters along with the calculated ΔT values are shown in Table 4.3. The thermal conductivity for carbon fibre was sourced from [30].

Component	Length (m)	Width (m)	Thickness (m)	Thermal Conductivity ($\mathrm{Wm^{-1}K^{-1}}$)	ΔT (K)
Foam	0.1	0.02	4.0×10^{-3}	40	37.5
Fibre	0.1	0.02	1.5×10^{-4}	1000	40.0

Table 4.3: ΔT comparison between foam and fibre. (Power output of 1.2 W through both foam and fibre).

The ΔT for the fibre component is now greater than that of the foam component, especially when considering a thickness of 150 microns. This suggests that, despite having a smaller thickness for the fibre component, a significantly higher coefficient of thermal conductivity can outweigh the impact of reduced thickness, resulting in an overall improvement in the thermal conductivity of the model. This underscores the significant influence of the direction of heat flow on the contributions from the fibre component and highlights the importance of accounting for such variations in thermal behaviour in the model. The combined ΔT for this model can then be calculated using equation (6) and the following relation,

$$P_{foam} = \frac{k_{foam} \times A_{foam} \times \Delta T_{foam}}{L} \;,\; P_{fibre} = \frac{k_{fibre} \times A_{fibre} \times \Delta T_{fibre}}{L} \tag{7}$$

$$P_{Total} = P_{foam} \;+\; P_{fibre} \;,\; \text{for} \;\; \Delta T_{foam} = \Delta T_{fibre} \tag{8}$$

$$\Delta T_{Total} = \frac{P_{Total} \times L}{k_{fibre} \times A_{fibre} \;+\; k_{foam} \times A_{foam}} \tag{9}$$

By employing equation (9), the combined ΔT for the model is calculated to be 20K as shown in Fig. 4.3 (green line). Which is lower than the individual ΔT values for both the fibre and foam components. The primary objective of this study is to assess whether the incorporation of fibre can enhance thermal conductivity within the module and whether adjustments to the module's design can increase the contribution from the fibre. This research aims to achieve a suitable operating temperature for the detector, aiming for a maximum temperature of 0°C, considering a coolant temperature of -30 °C. The results suggest that the fibre component has the potential to significantly impact the thermal behaviour of the module, and further design modifications could optimise its contribution to meet the desired operating temperature. The inclusion of just one layer of fibre in the simplified basic model has led to a decrease in the overall ΔT. However, with further refinements and the addition of a second layer of fibre, it is anticipated that the overall ΔT of the model can be adjusted to fall within the desired

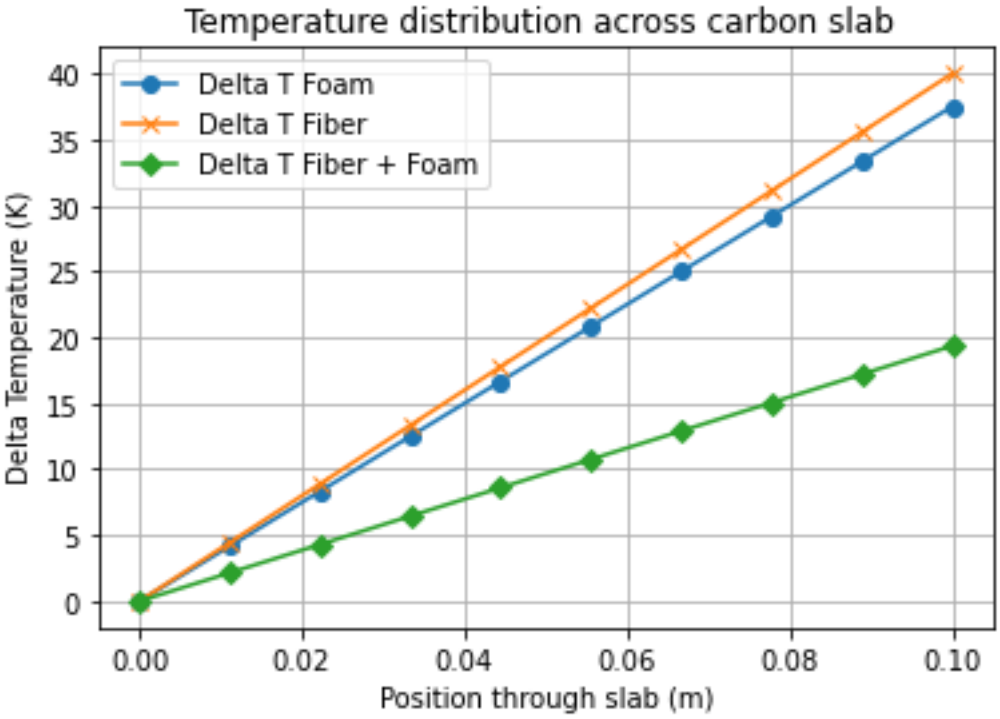

Figure 4.3:The figure illustrates the temperature rise (ΔT) across the carbon slab for three configurations: foam only, fibre only, and foam with fibre. The x-axis represents the position through the slab, and the y-axis represents the temperature difference relative to the inlet temperature.

range for operating the detector at temperatures around $0^{\circ}C$, as is shown in section 4.2.

4.2 Model Refinements and Thermal Performance Analysis

Up to this point in the calculations from the simplified model have indicated that both the foam and fibre components play a dominant role when heat flows through the length for the power of one chip, affecting the ΔT of the model. To make the model more realistic, a refinement has been introduced where the foam is sliced (dividing the foam into discrete segments) along the thickness, extending through the length of the foam, as shown in Fig. 4.4. By slicing the foam, the power distribution within the module becomes a function of length. This discretisation allows for a more accurate representation of temperature gradients within the foam, particularly at the boundaries between slices. Heat flow is assumed to occur continuously across these boundaries, with no thermal resistance or heat loss at the interfaces. Consequently, the ΔT is calculated separately for each individual slice, and these ΔT values are then integrated over the length as heat flows through the various slices.

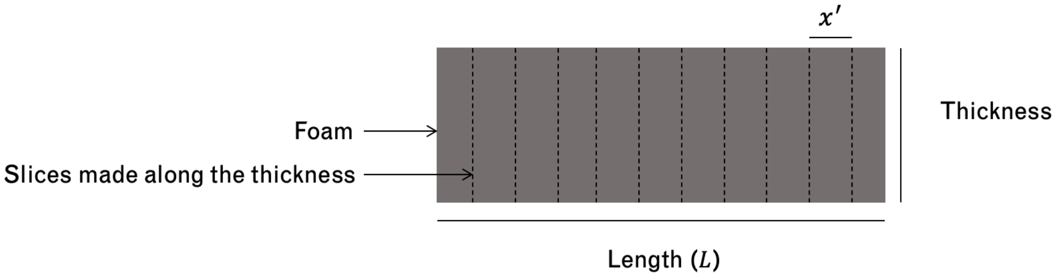

Figure 4.4: Schematic of Foam Discretisation for Thermal Analysis. The diagram illustrates the discretisation of the foam layer into multiple slices along its thickness (x') for improved thermal modelling. Each slice represents a control volume with uniform properties. Key dimensions include total length (L) and thickness.

To calculate the temperature difference over the foam while considering the power density through each slice and the length of each slice, Fourier's Law for heat transfer (5) is modified accordingly. The modified equation is derived as follows:

$$\int_{T_o}^{T_f} dT = \int_0^{x'} \frac{\rho(x) \times dx}{A \times k} \quad , \quad \Delta T = \frac{P}{A \times k}\int_0^{x'} dx \; - \frac{1}{A \times k}\int_0^{x'} \rho \times x \times dx \tag{10}$$

Simplifying, $\Delta T = \frac{\rho \times x'}{A \times k}(L - \frac{x'}{2})$ or $\Delta T = \frac{\rho \times x'^2}{2 \times A \times k}$ $(x' = L)$ (11)

In equation (10) and (11) $\rho(x)$ is the linear power density function, defined as $\rho(x) = P - \rho\,.\,x$, and $P = \rho\,.\,L$. Where P is the total power over the length of the foam slab and ρ is the linear power density (amount of heat generated per unit length) measured in units W/cm. Here the direction of L aligns with the length of the foam, directed towards the pipe, as illustrated in Fig. 4.1. x' represents the position of each slice on the foam, where $x' = 0$ corresponds to the beginning of the foam (right edge on Fig. 4.4). Using (11), the ΔT for the foam is calculated and the maximum ΔT at $(x' = L)$ is 93.75 K as shown in Fig. 4.5. The modification has resulted in a quadratic relationship between temperature and distance, with ΔT increasing as the distance grows. This updated value is notably higher than what was calculated previously, underscoring the dominant role of the foam in shaping the temperature distribution of the model.

In addition to the foam, the fibre with horizontal heat flow direction also plays a significant role, as demonstrated in the previous section. Using equation (11), the ΔT for the fibre was computed for both one and two layers of fibre, noting that the module consists of two layers. The results of these calculations are presented in Table 4.4 and visualised in Fig. 4.5.

Component	Maximum ΔT (K)
Foam	93.75
1 layer of Fibre	100
2 layers of Fibre	50

Component	Maximum ΔT (K)
Combined (Foam + 2 layers of Fibre)	32.60

Table 4.4: This table presents the maximum temperature difference (ΔT) for the foam, fibre (single and double layer), and the combined system. Values were calculated using Equation (11) and the material properties outlined in Table 4.3.

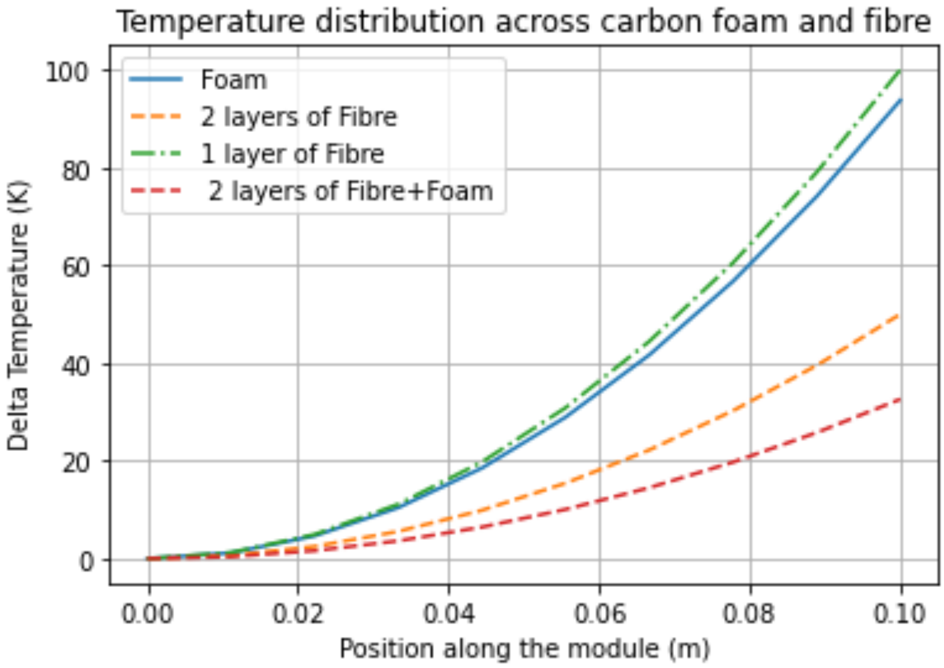

Figure 4.5: Temperature Distribution Along the Module for Different Material Configurations. The plot illustrates the temperature rise (ΔT) along the length of the module (x-axis) for various material configurations: foam only, one layer of fibre, two layers of fibre, and the combined foam and two-layer fibre system. The y-axis represents the temperature increase relative to the inlet temperature.

Building upon the analysis of the foam's thermal behaviour, the impact of adding fibre layers was investigated. With one layer of fibre, the temperature distribution follows a similar pattern and exhibits a comparable value to the foam. However, when the second layer of fibre is introduced, the temperature distribution is significantly reduced, leading to an improvement in the overall ΔT. The combination of both foam and fibre components yields an acceptable value for ΔT, highlighting that the incorporation of fibre, with its favourable thermal conductivity, contributes to an overall improved temperature difference. The incorporation of fibre significantly enhances the module's thermal performance by providing an additional heat dissipation pathway. This is evident in the reduced overall thermal resistance compared to the foam-only configuration. To determine the overall ΔT of the model, the contributions from all the components are combined, and the model is extended to be double-sided, as an extension towards a more realistic model. The resulting overall ΔT of the model, considering all components, is calculated to be 35.08K, which provides an estimate of the temperature difference within the module. Due to the inherent simplifications of the model, this value should be considered an approximation, as shown in Fig. 4.6. The discrepancy between the ΔT values in Table 4.4 and Figure 4.6 arises from the inclusion of additional components, such as glue, silicon, and the pipe, in the latter's calculations. The combined effect of these components adds 2.48K to the value compared to the combined value of just foam and two layers of fibre, as presented in Table 4.4.

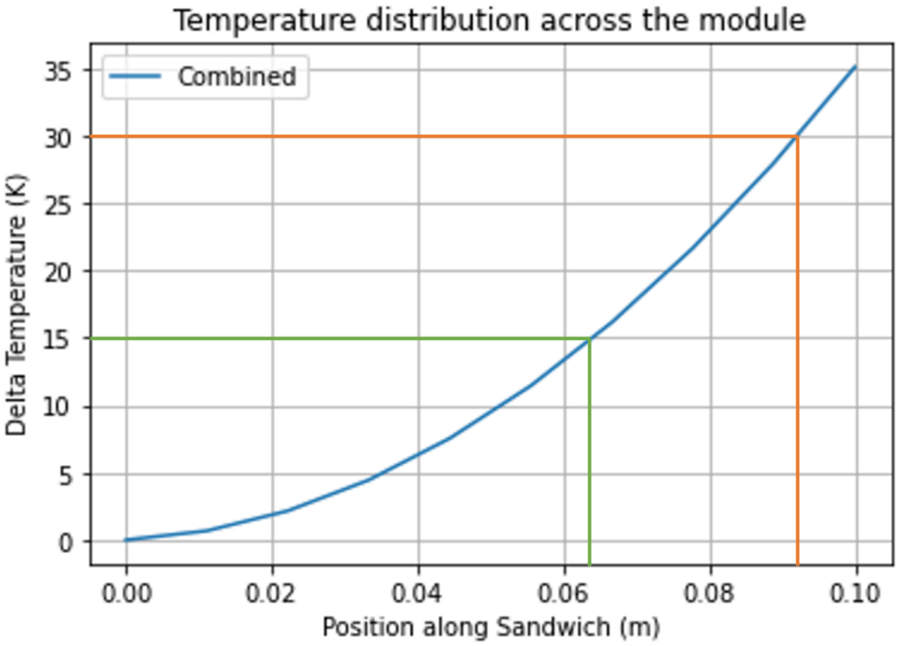

Figure 4.6: The plot illustrates the ΔT along the length of the module for the combined foam, fibre, and other components. The x-axis represents the position along the module, and the y-axis represents the temperature increase relative to the inlet temperature. Vertical markers indicate the optimal spacing for cooling pipes to maintain a chip temperature of 0°C.

Considering the overall temperature difference of 35.08K over a length of 0.1 meters, it can be concluded from Fig.4.6, that with chip dimensions of 20 mm x 20 mm, at least four chips on one side of the pipe can be effectively cooled to a temperature of 0°C, with a coolant temperature of -30°C. This implies that a total of approximately eight chips can be efficiently cooled using just one cooling pipe. The markers on Figure 4.6 indicate the optimal placement of cooling pipes to maintain sensor temperatures at 0 °C. Under nominal heat load conditions (0.15 W/cm^2), the green markers represent the cooling pipe positions with a spacing of approximately 0.18 m. Applying a safety factor of 2 to account for potential heat load increases (0.3 W/cm^2) necessitates a denser cooling pipe arrangement, as indicated by the orange markers with a spacing of approximately 0.13 m. To maintain effective cooling for a 0.50 m sample, it is determined that cooling pipes should be installed approximately every 0.18 m, which equates to approximately 3 cooling pipes for the full sample to ensure adequate temperature control. With the addition of a safety margin of a factor of two to the heat load, the overall ΔT would change to 15K changing the spacing to 0.13 m (from Fig. 4.6), which then means that for a 0.50 m sample, approximately 5 cooling pipes should be installed along the full length of the sample. Fig. 4.7 depicts a diagram illustrating one potential arrangement of chips on the module that can be cooled by a single pipe.

Further advancements and refinements to the thermal model are planned, and these improvements will involve:

Inclusion of Off-Chip Electronics: The model will be expanded to incorporate all off-chip electronics to provide a more comprehensive representation of the thermal behaviour of the entire system.
Non-Uniform Power Distribution: To account for realistic scenarios, the model will consider non-uniform power distribution, which reflects the actual power dissipation across different components and chips.
Overlap Considerations: Special attention will be given to addressing potential overlaps between chips and off-chip electronics on opposite sides of the module, as these interactions can influence temperature distribution and heat transfer within the system.

While the present model focuses on determining the optimal cooling pipe configuration based on heat dissipation from the silicon chips, it is essential to incorporate additional heat sources, such as DAQ electronics and environmental factors, in a more comprehensive thermal model. This expanded approach will enable a more accurate prediction of temperature distribution and facilitate the optimisation of thermal management strategies.

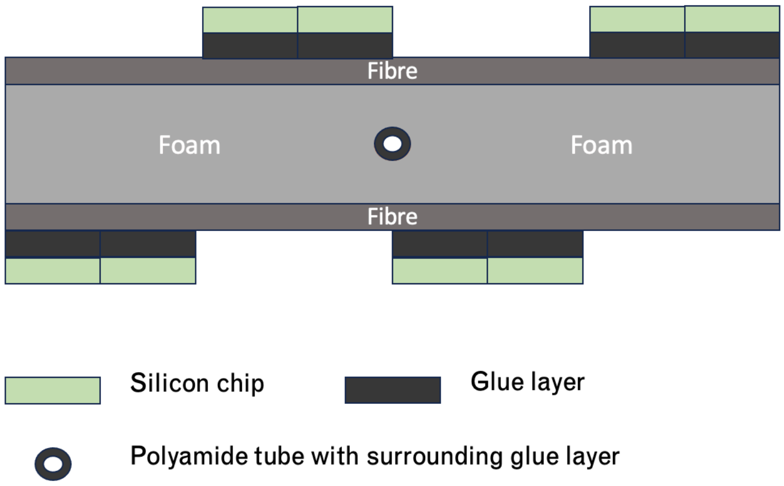

Figure 4.7: Optimised Chip Arrangement for Single-Pipe Cooling System. The figure depicts a proposed arrangement of eight silicon chips on the module, designed to be efficiently cooled by a single cooling pipe. The chips are organised in a staggered pattern to maximise heat dissipation and minimise thermal hotspots.

4.3 Summary

This chapter discusses the thermal characteristics of the Mighty Tracker prototype module. The primary objective is to establish a thermal model for predicting temperature distributions and optimising cooling strategies. A simplified thermal model is developed, considering heat transfer through the module's components. The model incorporates key parameters such as thermal conductivity, component dimensions, and power dissipation. Through calculations based on Fourier's Law, temperature differences within the module are estimated.

Key findings include:

- The significant impact of foam on overall thermal resistance.
- The beneficial effect of carbon fibre layers in enhancing thermal conductivity of the combined model.
- The estimation of optimal cooling pipe spacing based on calculated temperature distributions.

The chapter focuses on the importance of thermal management for the Mighty Tracker's performance.While the presented simplified model yields valuable preliminary data, it is acknowledged that its limitations warrant the inclusion of off-chip electronics and non-uniform power distribution in future iterations for enhanced accuracy.

{*Blank page*}

Chapter 5

X-Ray Tomography

Metrology detailed in chapter 3 primarily addresses surface quality control, but it is also essential to internally assess the assembly process. This can be achieved using X-Ray tomography to evaluate the module's internal quality and reliability.

X-Ray tomography is a technique that is used to create detailed three dimensional images of the internal structures of an object. The tomography involves an X-Ray source that emits a focused beam of X-rays. The process of X-ray tomography involves placing the object of interest between an X-ray source and a detector, as shown in Fig. 5.1. As the X-ray beams traverse through the object, their intensity is altered, either attenuated or absorbed, depending on the material's density and composition encountered by the beams. The detector, typically composed of scintillating crystals or solid-state detectors, measures the intensity of the X-ray beams after they have passed through the object.

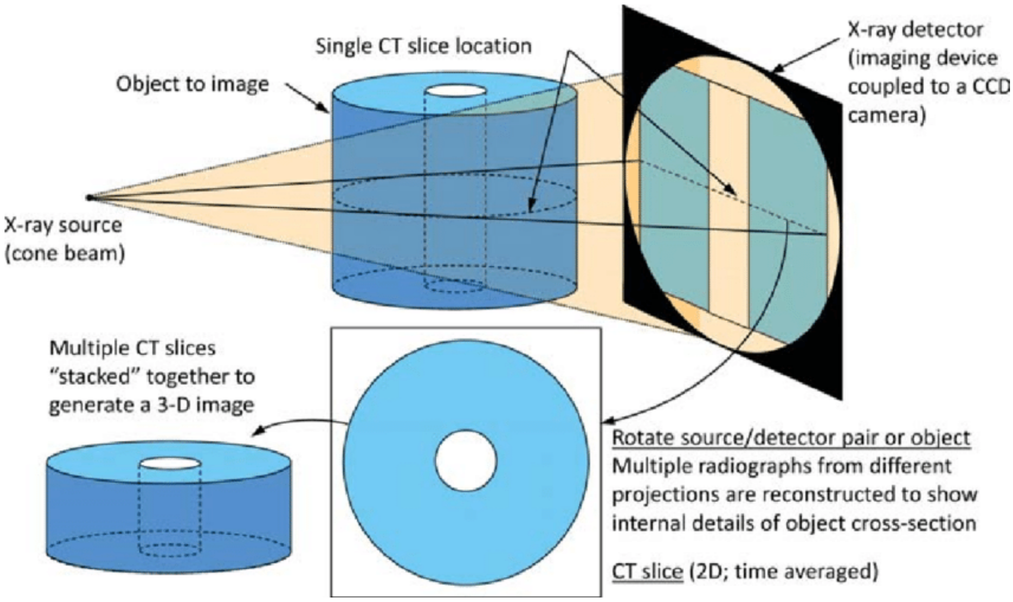

Figure 5.1: This figure illustrates the concept of X-ray tomography. A rotating X-ray source and detector acquire multiple projection images of an object from different angles. These projections are then reconstructed to create a 3D representation of the object's internal structure. [31].

To create a three-dimensional image, the object rotates around a fixed axis, capturing multiple images from various angles. While the object rotates, X-ray intensity measurements are collected at each angle, digitally recorded, and stored for subsequent analysis. Multiple CT (computed tomography) slices are then stacked together (as described in Fig. 5.1), leading to the reconstruction of a 3D image of the object. This visualisation provides a detailed representation of the internal structures within the object. Objects comprising materials of different densities, atomic number and thickness contribute to different levels of contrast to the final image, enhancing the distinction between various layers or components.

For the Mighty Tracker prototype modules, X-Ray tomography is employed to inspect and evaluate the internal structure of the modules. This inspection process is employed to identify and assess various features, including:

Carbon Fibre De-lamination: Whether there is any separation or de-lamination between the carbon fibre and the carbon foam components of the module.
Air Bubble Detection: The process is used to identify the presence of any air bubbles within the glue that may have formed during the assembly process. It also is used to check if the glue has been evenly spread throughout the sample, ensuring a consistent bond.
Cooling Tube Deformation: The process is used to examine the cooling pipe through the module, to check if there are any bends or kinks in the tube that would obstruct the flow of coolant.
Glue Thickness Variation: The 3D visualisation for the modules enables us to measure the thickness of the glue between the two halves of the module and observe how this thickness varies from one end to the other.

5.1 Methodology

The X-Ray tomography for the prototype modules was done at the Henry Mosley X-Ray Imaging Facility in the NXCT (National X-Ray Computed Tomography) lab at the University of Manchester. The machine used for the tomography was the Nikon Xtek High Flux Bay metrology system (Fig. 5.2). The CT machine is designed to perform tomography scans on a wide variety of objects, spanning from ancient bone fossils to intricate carbon-based materials. The machine is equipped with a versatile setup, including a 225kV power source for general imaging and a more powerful 320kV source for denser materials or higher resolution applications. This dual-source configuration provides flexibility in addressing a wide range of sample types. The onboard detector, with its 4000 x 4000 pixel resolution, captures detailed image data. The system's resolution spectrum spans from 2 to 119 microns, accommodating objects ranging from sub-millimetre components to larger assemblies. This substantial resolution range is primarily attributed to the combination of detector pixel size and the adjustable X-ray source parameters, such as voltage and current. For specialised measurements requiring higher X-ray flux, a rotating reflection target can be employed in conjunction with the 225kV power source. Furthermore, it offers the flexibility of higher-resolution scans, reaching up to 3-micron resolution. The high X-ray flux in the CT scanner is achieved through the utilisation of a static target with a power rating of 225W and a transmission target operating at a peak kilo voltage of 160kV. The system is also equipped with a 5-axis sample manipulator stage, which allows precise alignment of the object for intricate scans [31].

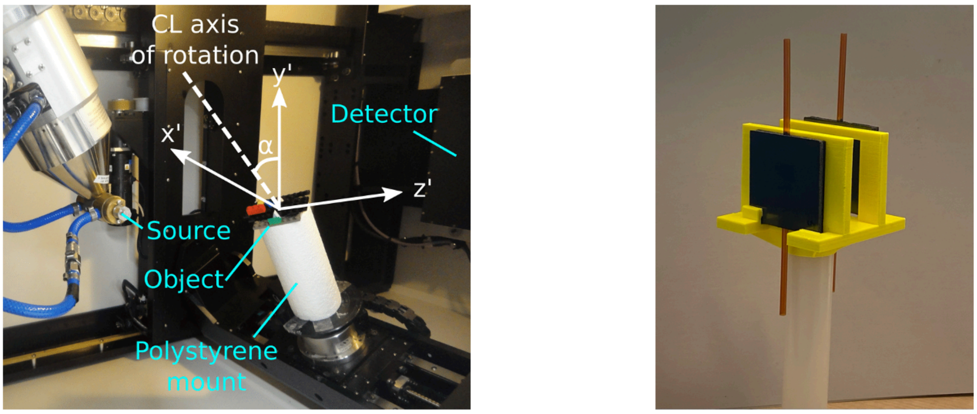

Nikon Xtek High Flux Bay

3D printed jig

Figure 5.2: CT machine used for the tomography (left), jig used to secure the modules to the mounting table (right)

To facilitate the tomography process, a custom jig was designed and 3D printed to accommodate the dimensions of the prototype modules. This jig enabled simultaneous scanning of two modules, as illustrated in Figure 5.2.
The jig lifts the modules high enough to get a top-down view of the cross-section of the modules along the y-axis, as shown in the CT slice in Fig. 5.3. The jig is firmly secured onto the mounting table, and the scanning process is initiated. During this process, the CT machine scans both of the modules simultaneously, generating CT slices that depict the internal structure of the two modules from the top to the bottom.

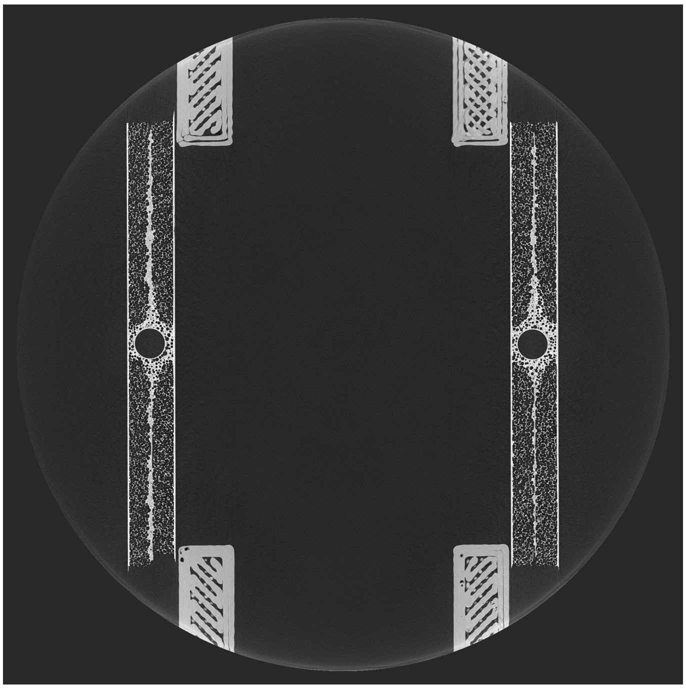

Figure 5.3: Top-down X-ray projection of two prototype modules (Sandwich 1 and Sandwich 2) arranged in a custom jig. The image reveals internal structures, including the carbon fibre layers, foam core, and potential voids or defects. The circular outline represents the module's outer boundary.

The CT slice depicted in Figure 5.3 provides a clear cross-sectional view of the two modules, highlighting how variations in density between the carbon foam, fibre, glue and pipe distinctly differentiate the different components within the modules. The captured images are saved and subsequently subjected to analysis to assess the internal composition of the modules. For this analysis, an image manipulation software called GIMP is employed. The measure tool from GIMP is utilised to conduct measurements of various components within the modules, including parameters like pipe diameter and glue thickness. These measured values are recorded and then subjected to further analysis using the Python. To convert the measurements obtained from GIMP, which are recorded in pixels, into real-world units, a scaling factor was determined. This scaling factor was calculated by measuring the length of module in pixels and then dividing that pixel value by the corresponding measurement taken with the SmartScope in millimetres. Table 5.1 presents all the critical parameters used in this analysis, including the scaling factor and other key measurement values.

Length of sample (mm)	40
Number of slices	2024
Pixel to mm conversion	1 pixel = 0.029 mm
Distance between slices (mm)	0.019

Table 5.1: Table of key parameters used in analysing X-ray tomography data.

5.1.1 Pipe Diameter Analysis and Verification

To ensure that the pipe is not deformed or bent in any section of the module, the diameter of the pipe was measured using GIMP for 40 equally spaced slices. The diameter was measured for each slice using the measure tool in GIMP, with a slice spacing of approximately 50 slices. Subsequently, distribution plots were generated for both modules, as shown in Fig. 5.4. The measured mean diameter for Module 1 was determined to be 2.698 mm with a standard deviation of 0.030 mm, while Module 2 exhibited a mean diameter of 2.696 mm with a standard deviation of 0.028 mm. As a point of comparison, the manufacturer's specification indicated an inner diameter of 2.67 mm for the pipe, accompanied by a wall thickness of 76 microns.

As illustrated in Figure 5.4, the measured values exhibit slight variations. This variability is a result of the manual measurement process, where a line is drawn across the pipe,

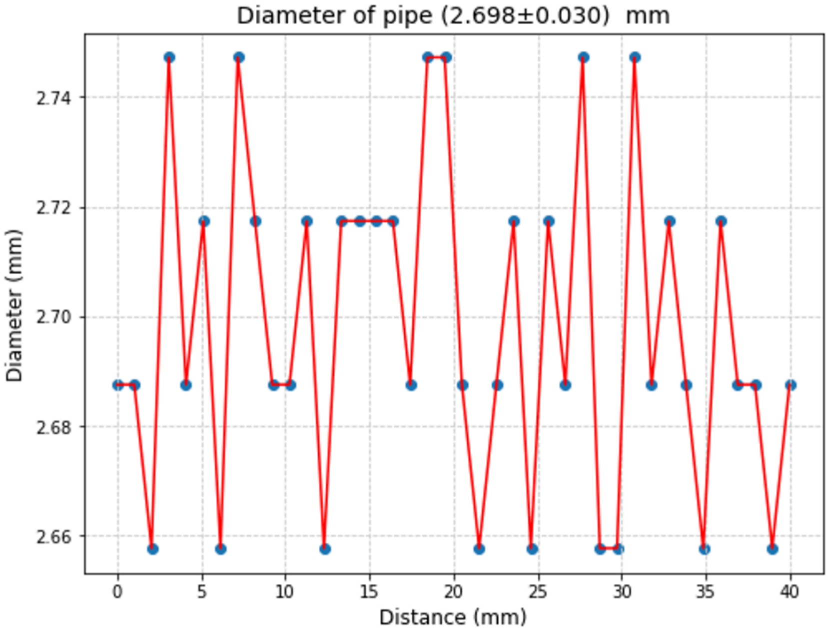

Sandwich 1

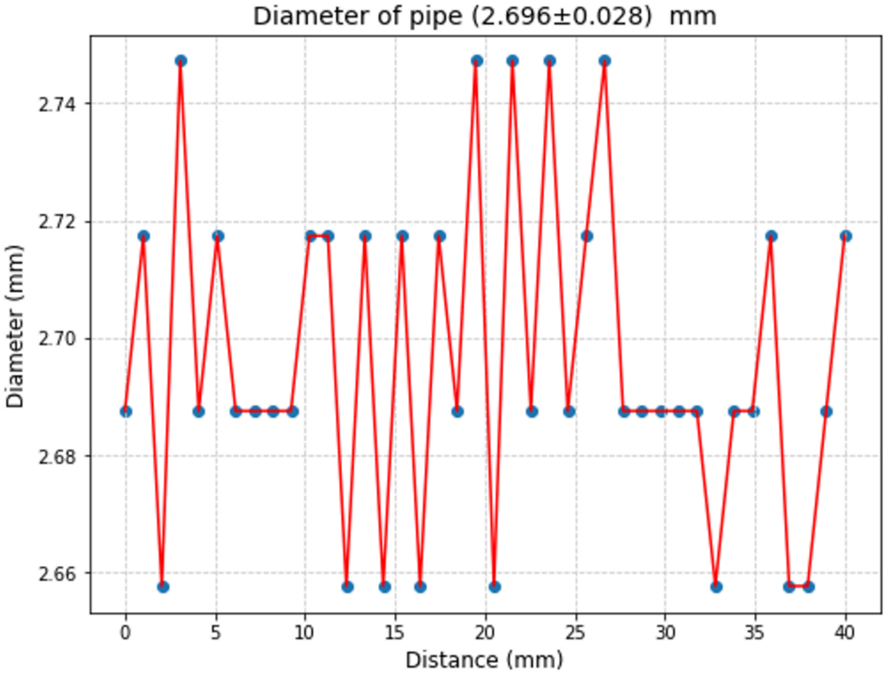

Sandwich 2

Figure 5.4: The plots illustrate the measured diameter of the pipe at equidistant intervals along the length of Sandwich 1 and Sandwich 2. The x-axis represents the distance along the pipe, while the y-axis indicates the measured diameter in millimetres.

and the measure tool records the pixel count within that line to determine the diameter in pixels.

The absence of any noticeable kinks or bends in the pipe for both modules suggests that there was no deformation or distortion of the pipe during the assembly process. Both plots exhibit minor deviations in pipe diameter, with a standard deviation of 0.03 mm for Sandwich 1 and 0.028 mm for Sandwich 2. While these variations are within the expected range for manufacturing tolerances. Overall, the data suggests that the pipe maintains a consistent diameter with minimal deviations, indicating good quality control in the manufacturing process.

5.1.2 Glue Thickness

Measuring the glue thickness across the entire length of the sample serves a dual purpose. Firstly, it allows for the assessment of the consistency of glue spread, both in proximity to the pipe and near the edges of the sample. Secondly, it provides insights into how the thickness of the glue varies as one moves vertically up the sample (along the pipe). The thickness is measured for 40 equally spaced slices along the length of the module. The measurement of glue thickness is conducted by assessing two specific areas: one near the pipe, where the glue is confined between the two halves of the module, and another near the edge of the module. It is important to note that the measurement near the pipe does not consider the spread of glue around the pipe, as demonstrated in Fig. 5.5. The glue thickness measurements are subsequently taken both near the pipe and near the edge of the module. The collected data is then used to generate distribution plots, which effectively illustrate the variation between these two sets of measurements. These plots provide a visual representation of how the glue thickness differs in these specific areas, offering valuable insights into the consistency of glue application within the module. The distribution is shown in Fig. 5.6.

Figure 5.6 illustrates the variation in glue thickness along the module, with distinct trends near the pipe and the edge. Statistical analysis reveals a mean glue thickness of 1.163 mm near the pipe and 0.373 mm near the edge. While there is a general trend of increasing glue thickness towards the edge, further analysis, including correlation and

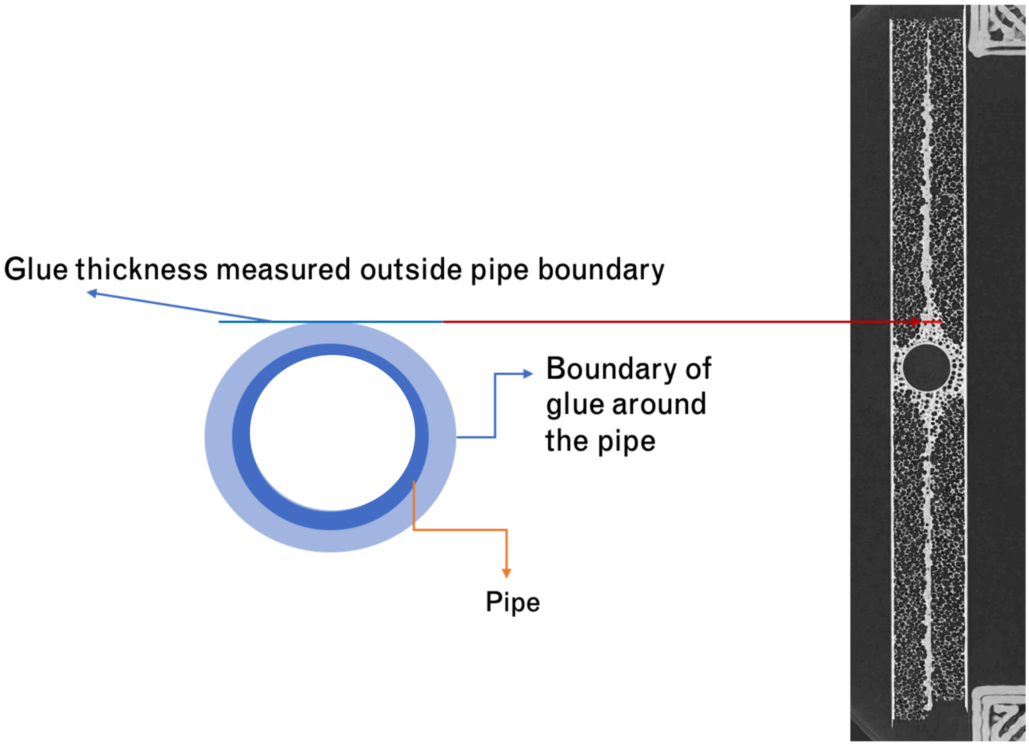

Figure 5.5: The figure illustrates the method for determining glue thickness around the pipe. The blue circle represents the pipe, surrounded by a layer of glue indicated by the shaded area. The red line and arrow demonstrate the measurement of glue thickness, taken perpendicularly from the pipe's outer boundary to the edge of the glue layer. The inset image provides a visual example of the measurement process on an actual sample

hypothesis testing, is required to establish a definitive relationship between glue thickness and position

To gain a more detailed understanding of the glue spread at the initial section (near the edges of the module) of the module tomography, where the difference in glue thickness between the edge and the pipe is minimal, a focused analysis is carried out. This analysis involves zooming in on this specific region and selecting 20 equally spaced slices. These slices are chosen from the point where the glue first becomes visible in the scans to the point where it reaches a consistent thickness. For each of these 20 slices, glue thickness measurements are conducted both near the pipe and near the edges of the module. Fig. 5.7 shows the distribution for the glue thickness at the start of the sample.

Fig. 5.7 provides an insight into the glue thickness measurements near the pipe and near the edges at the initial stages of the module tomography (first couple of slices when the tomography starts along the length of the pipe). Both measurements start at zero, indicating that initially, the glue has not yet entered these areas. Fig. 5.7 illustrates the glue thickness variation in the initial section of the module**.** While the glue thickness initially increases from zero at both the pipe and edge locations, a consistent difference emerges between the two measurements as the glue distribution progresses. The data suggests a higher concentration of glue near the pipe compared to the edge, resulting in a non-uniform glue distribution within the initial portion of the module.

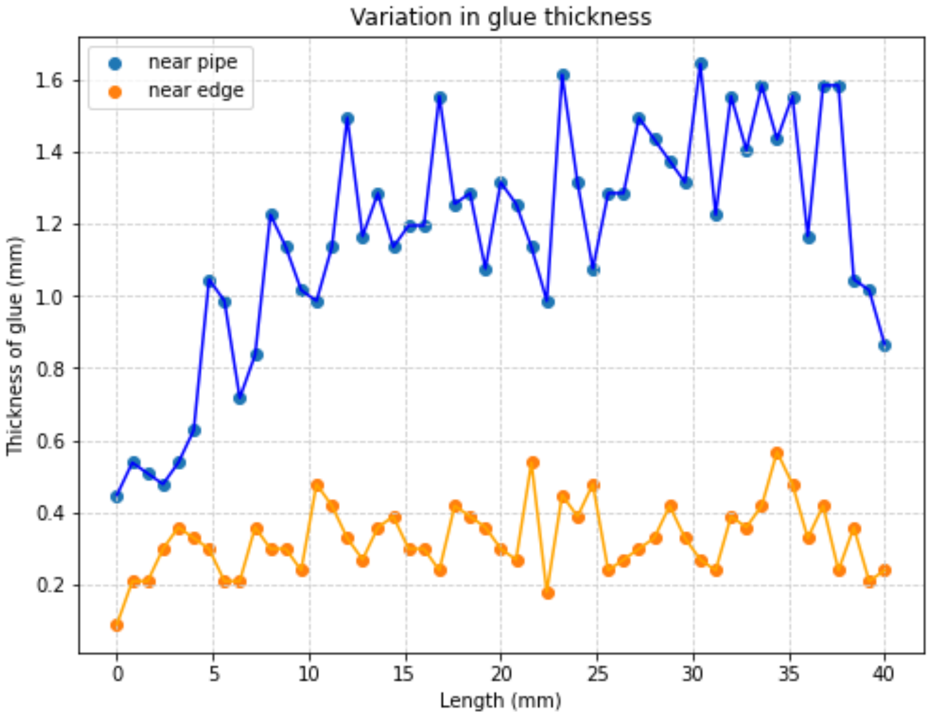

Figure 5.6: Scatter plot illustrating the variation in glue thickness (mm) along the length of the module. The data points represent measurements taken near the pipe (blue) and near the edge (orange) of the module. The x-axis represents the distance along the module length (mm), and the y-axis represents the corresponding glue thickness.

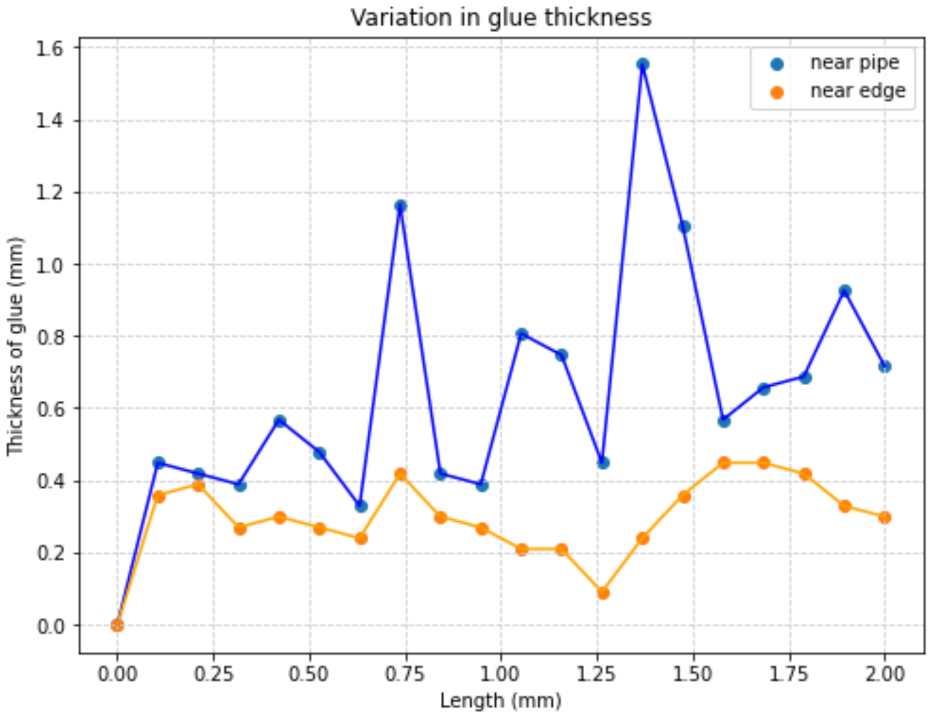

Figure 5.7: Scatter plot illustrating the variation in glue thickness (mm) along the first 2 mm of Sandwich 1. The x-axis represents the distance from the sample edge, while the y-axis indicates the measured glue thickness. Blue markers represent measurements near the pipe, and orange markers represent measurements near the edge. The plot highlights the non-uniform glue distribution within the initial section of the sample.

In summary, the analysis of glue concentration within the module reveals distinct characteristics. At the centre of the module, glue concentration is robust and relatively consistent. However, towards the beginning and end of the module, the glue concentration is weaker and displays inconsistencies. It is worth noting that these variations in glue thickness do not introduce any unexpected irregularities within the module. Despite the uneven glue thickness, there is no negative effect on the module's structural rigidity or strength. This is due to the effective bonding of the glue with the carbon foam; as long as it sufficiently bonds the two layers, the overall strength of the bond ensures ample structural rigidity. This suggests that the observed variations in glue distribution do not compromise the overall integrity of the module.

5.1.3 Analysis of Air Bubble Formation and Evolution

During visual analysis of the tomography images, an observation was made regarding the formation of an air bubble. This air bubble appeared at the beginning of the scan or near the edges of both modules and was consistently found at roughly the same slice in both cases, as shown in Fig. 5.8. The air bubble starts with a significant size and gradually diminishes in size as one progresses upward through the sample (from the edge of the module upwards along the length of the pipe). Ultimately, the bubble reaches a size that is consistent with the other glue bubbles present in the module. Fig. 5.8 effectively illustrates the dynamic changes in the size of this air bubble as it traverses through the module.

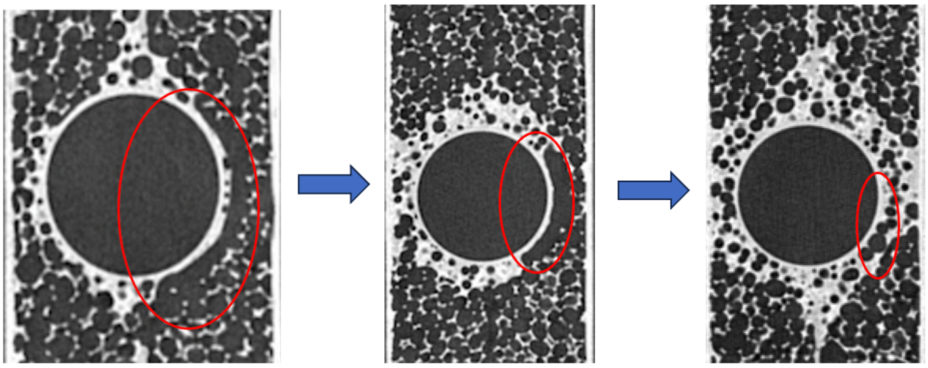

Bubble starts at this size.

Shrinks down as we move up the sample.

At the end, it becomes small and remains at constant size.

Figure 5.8: The figure depicts the progressive change in air bubble shape and size along the length of the sample. The initial circular bubble (left) undergoes deformation and reduction in size (middle) before stabilising into a smaller, circular shape (right).

To comprehensively assess the size variation of the air bubble throughout the module, a zoomed in analysis was conducted. This analysis involved selecting 20 evenly spaced slices, starting from the point when the air bubble first appeared and concluding when it reached a consistent size similar to other glue bubbles within the module. To measure the size of this air bubble, the measuring tool in GIMP was employed. Given the asymmetric shape of the larger bubble, as evident in Fig. 5.8, a series of lines were measured within the bubble, as shown Fig. 5.9, and the length was calculated as the sum of these line lengths. For smaller bubbles, their size was simply measured as the approximate diameter. This detailed measurement process allowed for a thorough examination of how the air bubble's size evolved within the module.

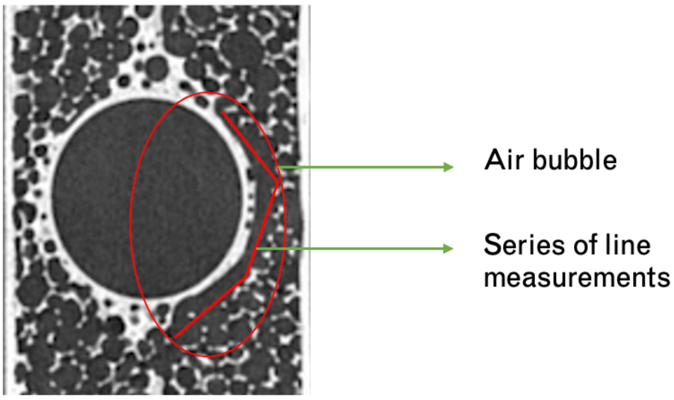

Figure 5.9: Measurement of Air Bubble Dimensions. The red outline approximates the irregular shape of the bubble, while the series of red lines illustrate the method for calculating its approximate area.

Fig. 5.10 illustrates the size variation of the air bubble along the length of both modules. The analysis of the air bubble's size reveals interesting differences between module or sandwich 1 and module or sandwich 2. Initially, when the bubble first appears, its size is larger in sandwich 1, measuring 3.278 mm, compared to 2.293 mm in sandwich 2. However, as the bubble progresses and becomes consistent with the size of other glue bubbles, it shrinks down to 0.447 mm in both cases. The span of this air bubble encompasses 145 slices, considering the conversion factor for the distance between each slice from Table 5.1 this equates to a length of approximately 2.75 mm. Given that the sample is 40 mm long, it means that the bubble occupies approximately one-fifteenth of the sandwich's length. Furthermore, the analysis shows a steady decline in the bubble's size from its initial appearance to when it stabilises and becomes consistent with the other glue bubbles with a size of the bubble as 0.4 mm.

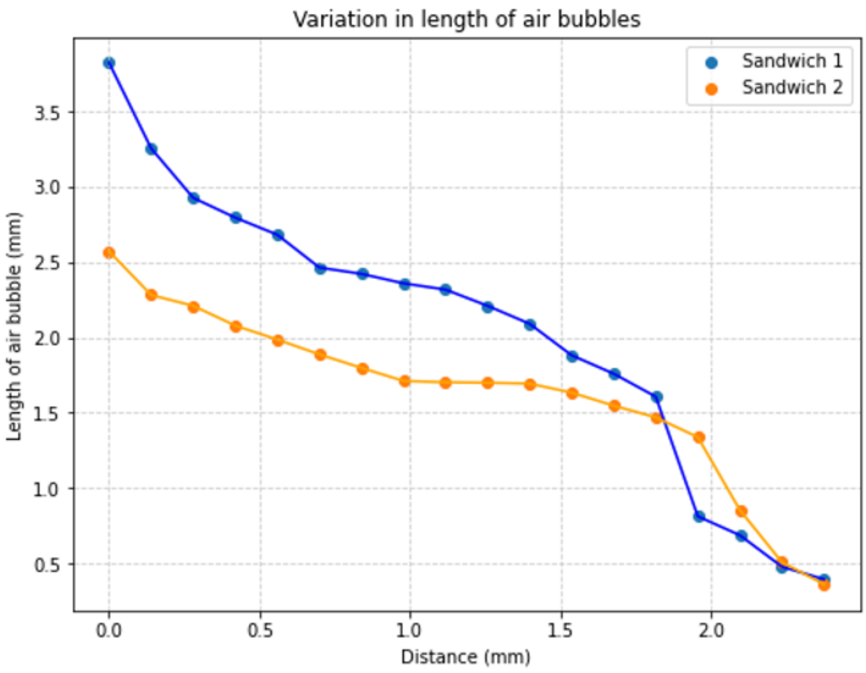

Figure 5.10: Scatter plot illustrating the change in air bubble length (mm) as a function of distance along the module (mm) for Sandwich 1 and Sandwich 2. The data reveals a decreasing trend in air bubble length for both samples, with Sandwich 1 exhibiting a larger initial bubble size compared to Sandwich 2.

To comprehensively compare the air bubble with the rest of the glue bubbles within the module, a detailed analysis was conducted. This analysis involved measuring the air bubble once more, but this time, 40 evenly spaced slices were selected to cover the entire length of the sample. The goal was to assess how the air bubble's size and characteristics compare to the other glue bubbles and to identify any other notable large bubbles within the module. Fig. 5.11 provides a distribution plot that illustrates the lengths of both the air bubble and the glue bubbles within the module. The plot demonstrates the air bubble's initial large size, followed by a significant reduction to approximately 0.5 mm. Subsequently, the glue bubbles align with this size and maintain it throughout the distribution.

Notably, there are instances where the bubble size increases as seen in Fig. 5.11 at approximately 8 mm, 18 mm and 23 mm. These points correspond to situations where multiple bubbles appear to combine, forming larger conglomerates as shown in Fig.

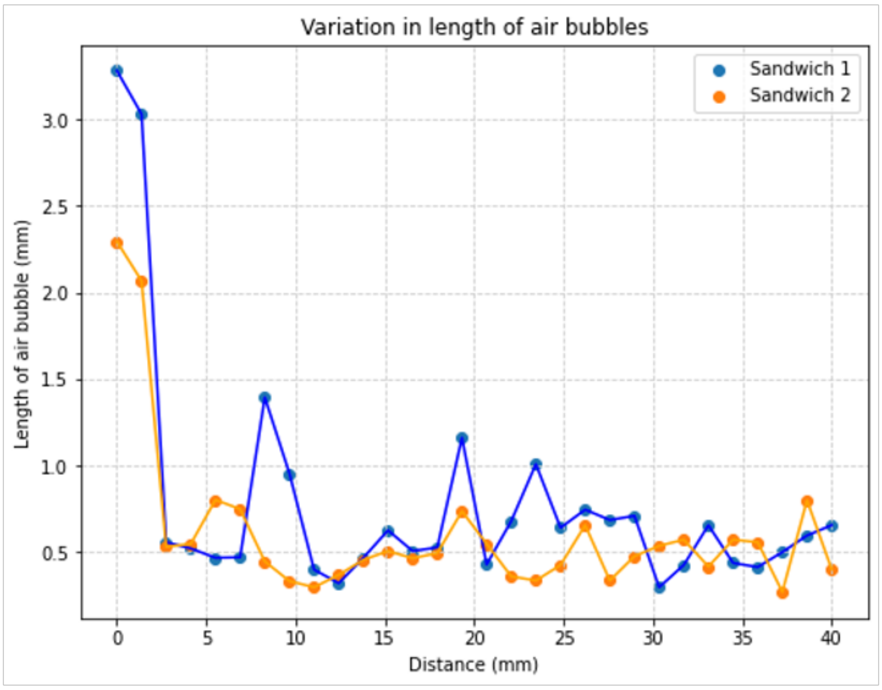

Figure 5.11: Scatter plot illustrating the transition of air bubbles into glue-like inclusions along the length of the module for Sandwich 1 (blue) and Sandwich 2 (orange). The plot demonstrates a decrease in air bubble size, culminating in the formation of smaller, glue-like structures.

5.12. While these combined bubbles are not as large as the air bubble present at the start of the module, they do occasionally emerge, likely as a result of the glue-spreading process during module assembly. Analysis of the glue bubbles within the modules reveals distinct patterns**.** While both sandwiches exhibit a general trend of decreasing bubble size along the module length, Sandwich 1 displays greater variability with instances of bubble coalescence and larger initial bubble formation. The presence of these larger bubbles in Sandwich 1 suggests potential inconsistencies in the glue application process. Overall, the data indicates a need for process refinements to minimise air bubble formation and achieve a more uniform glue distribution. While the presence of a rough foam surface may contribute to air bubble entrapment, other factors such as incomplete glue mixing, improper application techniques, or environmental conditions during the curing process could also influence bubble formation. For sandwich 2, the glue bubbles exhibit a relatively uniform distribution in terms of size. In contrast, for sandwich 1, there are several notable high spots, but the majority of the glue bubbles fall within the ±0.5 mm size range.

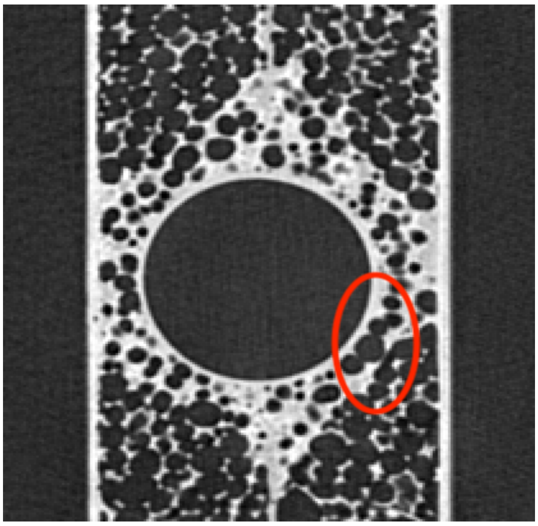

Figure 5.12: Cross-sectional X-ray tomography image highlighting the formation of a large air bubble through the merging of multiple smaller bubbles. The red circle indicates the region of interest, showcasing the bubble's growth and interaction with surrounding structures.

5.2 Summary

The X-Ray tomography process has played a pivotal role in thoroughly examining the internal structure of the modules, ensuring the absence of significant deformations post-assembly. The results of the tomography have yielded several important findings:

No De-lamination: The tomography results confirm the absence of any de-lamination between the foam and fibre components, indicating a sound bond between these materials.

Cooling Pipe Integrity: It is evident that the cooling pipe has remained undistorted both during and after the assembly procedure, maintaining its structural integrity.

Glue Concentration: The concentration of glue is observed to be centred around the module's core, with non-uniform distribution at the edges. However, this non-uniformity does not appear to impact the bonding strength between the two halves of the module.

Air Bubble: A noteworthy finding is the presence of an air bubble that has formed during the curing process of the modules. This issue can be avoided by applying the glue evenly during the assembly process. Analysis of the glue application process suggests that a more uniform glue distribution along the pipe length could potentially improve bond quality and reduce air bubble formation. Future studies will investigate the impact of different glue application techniques on overall module performance.

Overall, the tomography analysis provides valuable insights into the internal structure of the module. The observed variations in glue thickness warrant further investigation to optimise the bonding process and ensure consistent adhesive distribution. The detected air bubble represents a potential assembly issue, the absence of other significant defects suggests a generally robust assembly process. The use of tomography has proven essential for identifying this anomaly, highlighting its role in quality control. Further investigation into the root cause of the air bubble formation is recommended to optimise the manufacturing process and prevent similar defects in future modules.

{*Blank page*}

Chapter 6

Conclusion

The development and characterisation of the Mighty Tracker prototype modules required a multifaceted approach encompassing metrology, thermal analysis, and X-ray tomography. Precision metrology ensured the adherence to dimensional tolerances for the co-cured carbon foam and fibre components. Thermal simulations established baseline temperature distributions and identified critical cooling requirements, necessitating approximately five cooling pipes spaced at 0.18 m intervals along a 0.5 m module. X-ray tomography provided valuable insights into internal assembly quality, revealing details about glue distribution and the presence of minor anomalies such as air bubbles. Building upon these foundational studies, ongoing research focuses on finalising the Inner Tracker design, including pixel layout optimisation and refined cooling strategies. By addressing challenges such as air bubble formation and optimising glue distribution, the overall performance and reliability of the modules can be further enhanced.

Continued R&D efforts are underway to finalise the details of the Inner Tracker design such as the layout of silicon pixels on modules. Additional simulation studies and detector prototyping will further improve and validate the design. Once completed, it is expected that the Inner Tracker and the broader Mighty Tracker system can achieve world-leading tracking precision even at the unprecedented collision rates and integrated luminosities planned for the High-Luminosity LHC during Runs 5 and 6 in the late 2020s and 2030s. These studies are playing a critical role in maximising the groundbreaking physics output anticipated from the upgraded LHCb experiment.

{Blank page}

Bibliography

[1] "The Standard Model.," CERN. https://home.cern/science/physics/standard-model

[2] R. Mann (2010). "25". An Introduction to Particle Physics and the Standard Model. CRC Press. ISBN 978-1-4200-8298-2.

[3] commons.wikimedia.org, "Symmetry in quantum mechanics." https://en.wikipedia.org/w/index.php?title=Symmetry_in_quantum_mechanics&oldid=1187988095, 11, 2023

[4] commons.wikimedia.org, "CP violation," Wikipedia. https://en.wikipedia.org/wiki/CP_violation, 11, 2023

[5] commons.wikimedia.org, "T-symmetry." https://en.wikipedia.org/w/index.php?title=T-symmetry&oldid=1188389647, 11, 2023

[6] commons.wikimedia.org., "Chirality (physics)." https://en.wikipedia.org/w/index.php?title=Chirality_(physics)&oldid=1174316318, 11, 2023

[7] Pich, A. "CP Violation." CERN-TH-7114/93. Theory Division, CERN, Dec. 1993. ICTP Ser. Theor. Phys. 10 (1993): 14-42. CERN Document Server. https://cds.cern.ch/record/256553

[8] Virdee, T.S., "Beyond the standard model of particle physics.," *Philosophical Transactions of the Royal Society A: Mathematical, Physical and Engineering Sciences* 374, no. 2075 (2016): 440-51. https://doi.org/10.1098/rsta.2015.0259

[9] Evans, L. and Bryant, P. (2008). LHC Machine. *Journal of Instrumentation*, 3(08), pp.S08001–S08001, https://doi.org/10.1088/1748-0221/3/08/s08001

[10] La Rocca, P. and F. Riggi, "The upgrade programme of the major experiments at the Large Hadron Collider," *Journal of physics*, no. 515 (2014): 012012–12, https://doi.org/10.1088/1742-6596/515/1/012012

[11] "Facts and figures about the LHC | CERN (2019)“ https://home.cern/resources/faqs/facts-and-figures-about-lhc, 11, 2023

[12] ATLAS Collaboration, Aamodt, K et al., "The ATLAS Experiment at the CERN Large Hadron Collider," *Journal of Instrumentation* 3, no. 08 (2008): S08003, https://dx.doi.org/10.1088/1748-0221/3/08/S08003

[13] CMS Collaboration, S. Chatrchyan et al., "The CMS experiment at the CERN LHC," *Journal of Instrumentation* 3, no. 08 (2008): S08004, https://dx.doi.org/10.1088/1748-0221/3/08/S08004

[14] ALICE Collaboration, Aamodt, K et al., "The ALICE experiment at the CERN LHC. Journal of Instrumentation,"3(2008). https://dx.doi.org/10.1088/1748-0221/3/08/S08002

[15] LHCb Collaboration, Akiba, K et al., "The LHCb Detector at the LHC," *Journal of Instrumentation* 3, no. 08 (2008): S08005, https://dx.doi.org/10.1088/1748-0221/3/08/S08005

[16] Elsasser, C., "LHCb bb production angle plots.." https://lhcb.web.cern.ch/lhcb/speakersbureau/html/bb_ProductionAngles.html}{https://lhcb.web.cern.ch/lhcb/speakersbureau/html/bb_ProductionAngles.html

[17] Svihra, P. (2021). Developing a silicon pixel detector for the next generation LHCb experiment [Report No. CERN-THESIS-2021-309]. University of Manchester. https://cds.cern.ch/record/2806219

[18] LHCb Collaboration, "The LHCb upgrade I,"(2023). https://arxiv.org/abs/2305.10515. doi: 10.48550/arXiv.2305.10515

[19] LHCb Collaboration. (2021). Framework TDR for the LHCb Upgrade II: Opportunities in flavour physics, and beyond, in the HL-LHC era (Report No. CERN-LHCC-2021-012, LHCB-TDR-023). CERN.https://cds.cern.ch/record/2776420

[20] Aberle, O. et al. (2020). High-Luminosity Large Hadron Collider (HL-LHC): Technical design report (CERN Yellow Reports: Monographs). CERN. doi: 10.23731/CYRM-2020-0010.

[21] LHCb Collaboration, CERN (Meyrin (2021). *"Framework TDR for the LHCb Upgrade II Opportunities in flavour physics, and beyond, in the HL-LHC era"*. CERN Document Server. https://cds.cern.ch/record/2776420?ln=en, 10, 2023.

[22]Bellato, M., et al. "A PCIe Gen3 Based Readout for the LHCb Upgrade." *Journal of Physics: Conference Series* vol. 513, no. 1, 2014, p. 012023. doi:10.1088/1742-6596/513/1/012023

[23] Murray, D., "Developing silicon pixel detectors for LHCb: constructing the VELO Upgrade and designing a MAPS-based tracking detector.," (University of Manchester, 2021). https://cds.cern.ch/record/2808484?ln=en, 11, 2023

[24] EPFL, *The LHCb Mighty Tracker (Exploring a conceptual tracker design combining scintillating fibres and HV-MAPS detectors)*, 2020

[25] Schöning, A, et al., *MuPix and ATLASPix -- Architectures and Results.*, 2020. https://doi.org/10.48550/arXiv.2002.07253

[26] Augustin, H et al., CERN, *Preliminary Specification of a HV-CMOS Pixel Chip for LHCb Upgrade II*. Geneva, 2020. https://indico.cern.ch/event/901742/contributions/3796706/attachments/2008892/3355834/ChipSpecifications_10.pdf, 11, 2023.

[27] Huth, L., "A High Rate Testbeam Data Acquisition System and Characterization of High Voltage Monolithic Active Pixel Sensors," (University of Heidelberg, 2019). https://dx.doi.org/10.11588/heidok.00025785

[28]"OGP SmartScope ZIP 300." https://www.ogpnet.com/products/metrology-systems/multisensor-metrology-systems/smartscope-video-mult-sensor-systems/smartscope-zip-multisensor-systems/smartscope-zip-300/, 11, 2023

[29] commons.wikimedia.org, "Thermal conduction." https://en.wikipedia.org/w/index.php?title=Thermal_conduction&oldid=1195218525, 11, 2023

[30] Gomez Marzoa, M., "Innovative low-mass cooling systems for the ALICE ITS Upgrade detector at CERN," (Ecole Polytechnique, 2016). https://cds.cern.ch/record/2231119?ln=en, 11, 2023

[31] "Nikon Xtek High Flux Bay." https://nxct.ac.uk/facilities/manchester/high-flux-bay/, 11, 2023

[32] "CERN AC (1998). Layout of ATLAS." https://cds.cern.ch/record/39038, 11, 2023

[33] Heindel, T., "A Review of X-Ray Flow Visualization With Applications to Multiphase Flows," *Journal of Fluids Engineering* 133(2011): 074001. https://doi.org/10.1115/1.4004367

[34] Sakuma, T. and T. McCauley, "Detector and Event Visualization with SketchUp at the CMS Experiment," *Journal of Physics: Conference Series* 513, no. 2 (2014): 022032, https://dx.doi.org/10.1088/1742-6596/513/2/022032 (accessed 2014/06/11)

[35] Tauro, A., "ALICE Schematics," (CERN Document Server: 2017). https://cds.cern.ch/record/2263642, 10, 2023

[36] commons.wikimedia.org, "Standard Model.," Wikipedia. https://en.wikipedia.org/wiki/Standard_Model, 10, 2023

[37] commons.wikimedia.org, "Standard Model Feynman Diagram Vertices.png - Wikipedia."https://en.wikipedia.org/wiki/File:StandardModelFeynmanDiagramVertices.png, 10, 2023

[38] 3M. 1998. *3M™ Novec™ 7100 Engineered Fluid*. https://multimedia.3m.com/mws/media/199818O/3m-novec-7100-engineered-fluid.pdf?&fn=prodinfo_nvc7100_R1.pdf.

[39] U.S. Department of Energy. (n.d.).DOE Explains...the Standard Model of Particle Physics. https://www.energy.gov/science/doe-explainsthe-standard-model-particle-physics